

FEMTOSECOND DYNAMICS OF MOLECULAR REACTIONS AT METAL SURFACES

Richard Finlay and Eric Mazur

Department of Physics
Harvard University
Cambridge, MA 02138

ABSTRACT

These lectures are an introduction to current research into photo-induced chemical reactions at metal surfaces. After an introduction to some qualitative quantum mechanics, we discuss the electronic and optical properties of metals, beginning from an introductory level. The Drude model is described in detail and then optical properties of matter are developed more completely by introducing band structures. The physics governing adsorption of reactants at a metal surface and other fundamental concepts in surface science are introduced. We describe the interaction with a subpicosecond laser pulse with a metal surface in preparation for discussion of some recent photochemistry experiments using subpicosecond laser pulses. The experiments address the nature of the photo-excited electrons that are responsible for chemical reaction of the adsorbates.

I. THE QUANTUM MECHANICS AND SPECTROSCOPY OF ATOMS

This section provides a brief overview of some fundamental concepts from quantum mechanics which are relevant to spectroscopy and molecular dynamics. The emphasis is on developing a physical interpretation of the Schrödinger equation. Introductions to quantum mechanics that approach the subject in more detail through mathematical formalism[1] or by following the historical development of the subject[2] are available.

I. A. The Schrödinger equation

The justification for quantum mechanics is its agreement with experiment, and the consistency and elegance of the mathematical formalism. Nevertheless, it is instructive to provide a motivation based on classical mechanics. In classical mechanics the energy of a particle in an external potential $U(x)$ is

$$E = \frac{p^2}{2m} + U(x), \quad (1)$$

where p is the momentum and m is the mass of the particle. In quantum mechanics p and x are interpreted as quantum mechanical operators. Let's view x as proportional to an operator which means *multiply by the position* and p as proportional to an operator which means *take the derivative with respect to x* . These definitions are consistent with our intuition that the momentum specifies the rate of change of position. When the transformation

$$p \rightarrow -i\hbar \frac{d}{dx} \quad (2)$$

is applied to (1) the classical expression for the total energy is transformed into an operator expression. This operator is called the Hamiltonian, H :

$$\frac{p^2}{2m} + U(x) \rightarrow \frac{1}{2m} \left[-i\hbar \frac{d}{dx} \right]^2 + U(x) = -\frac{\hbar^2}{2m} \frac{d^2}{dx^2} + U(x) \equiv H. \quad (3)$$

The function that these operators act on is called the wavefunction, Ψ . The result is the time-independent Schrödinger equation:

$$H\Psi = E\Psi. \quad (4)$$

There is also a time-dependent Schrödinger equation. The following expression describes the time rate of change of the wavefunction in terms of the now time-dependent Hamiltonian[1]

$$H\Psi = i\hbar \frac{\partial \Psi}{\partial t}. \quad (5)$$

The time-dependent Schrödinger equation reduces to (4), the time-independent Schrödinger equation if the potential energy is independent of time: $U = U(x)$. To see this, write the wavefunction, Ψ , as a product of a time-dependent and a time-independent part:

$$\Psi(x, t) = \Psi(x)\theta(t). \quad (6)$$

Substituting (6) into (5), the equation separates into an expression with only spatial dependence on the left side, and only time dependence on the right side:

$$-\frac{\hbar^2}{2m} \left(\frac{1}{\Psi} \frac{d^2 \Psi}{dx^2} \right) + U(x) = i\hbar \frac{1}{\theta} \left(\frac{d\theta}{dt} \right). \quad (7)$$

Because the right side is a constant independent of x , the left side must also be independent of x , and is therefore constant. Call the constant E .

$$-\frac{\hbar^2}{2m} \nabla^2 \Psi + U(x)\Psi = E\Psi \quad (8)$$

$$i\hbar \frac{d\theta}{dt} = E\theta \quad (9)$$

The symbol ∇^2 represents the second derivative with respect to x . The first equation is simply the time-independent Schrödinger Equation 4 which justifies using the letter E for the constant. The second equation has a trivial solution:

$$\theta(t) = Ce^{-iEt/\hbar}. \quad (10)$$

What does this mean? In a time-independent potential, the time-dependence of the wavefunction is simply a rotation of the (complex) phase of the wavefunction. The frequency of this rotation is determined by the energy.

The product $\Psi(x,t)^* \Psi(x,t)$ is very important in quantum mechanics. Born interpreted it as a probability density; the probability of finding a particle described by wavefunction $\Psi(\vec{r},t)$ within a volume element $d\vec{r}$ of \vec{r} is

$$\Psi(\vec{r},t)^* \Psi(\vec{r},t) d\vec{r}. \quad (11)$$

According to this interpretation, the wavefunction must be normalized to reflect the requirement that the particle is certainly somewhere in space:

$$\int \Psi(\vec{r},t)^* \Psi(\vec{r},t) d\vec{r} = 1. \quad (12)$$

The integral in Equation 12 is over all space. In the special case of a particle in a time-independent potential, Equation 10 contains all the time-dependence of the wavefunction. The product $\Psi(x,t)^* \Psi(x,t)$ is constant in time and so the wavefunction is called a stationary state.

The interpretation of $\Psi(x,t)^* \Psi(x,t)$ as a probability density places constraints on Ψ . It must be single-valued. It may not be infinite (unless it is infinite in only an infinitesimally small region of space). Furthermore, since the wavefunction is a solution of a second order differential equation (the Schrödinger equation) it must be continuous. If the potential is not too pathological then the first-derivative of Ψ is also continuous.

I. B. Origin of energy quantization

Rewriting the Schrödinger equation, we see that it specifies the curvature of the wavefunction:

$$\nabla^2 \Psi = \frac{2m}{\hbar^2} [U(x) - E] \Psi. \quad (13)$$

Where $U(x) = E$ the curvature of the wavefunction is zero. In other regions, the sign of the curvature is determined by the signs of both Ψ and $U(x) - E$.

The meaning of the Schrödinger equation may be clarified by making qualitative sketches of possible solutions to Equation 13, using the equation to specify the sign of the curvature of Ψ . The left side of Figure 1 shows a potential energy surface and beneath it, two trial wavefunctions of energy E which have the same value at $x = x'$. Between x' and x'' , both wavefunctions have downward curvature because Ψ is positive, and $E > U(x)$. Just beyond x'' , Ψ is still positive but $E - U(x)$ changes sign. The curvature of both wavefunctions becomes upward. The upward curvature causes Ψ_A to diverge. Wave function Ψ_B soon passes below zero; Ψ_B changes sign, the curvature again becomes downward, and the wavefunction diverges downwards. Wavefunctions Ψ_A and Ψ_B are not acceptable because they are not normalizable. A wavefunction (not shown) with slope at x' between that of Ψ_A and Ψ_B would satisfy Equation 13 without diverging by tending to zero beyond x'' .

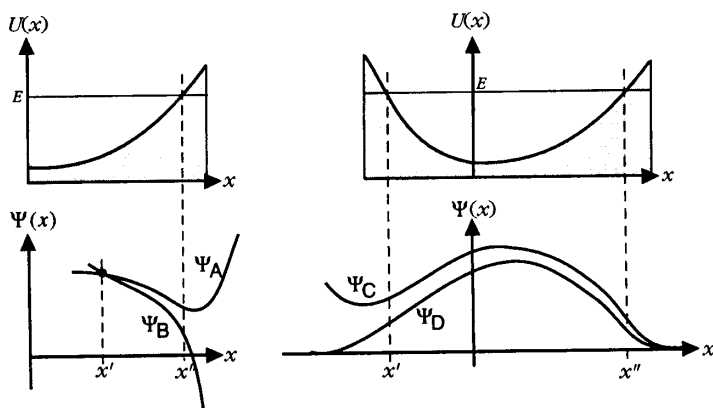


Figure 1 Qualitative trial wavefunctions of energy E for two potentials. Wavefunctions A, B and C are not acceptable because they diverge, and are not normalizable. D is a correct wavefunction. Starting with a trial energy, slope and value at x' , the second derivative of the wavefunction is constrained by the Schrödinger equation. After [2].

The right side of Figure 1 demonstrates that a potential energy surface bounded on both sides further constrains the wavefunctions. Two wavefunctions are sketched. Both tend towards zero for positive x . However Ψ_C diverges on the left side. Wavefunction Ψ_D is normalizable. It has finite extent in the x -direction and is called a bound-state wavefunction. It turns out that normalizable wavefunctions exist only for special values of the energy: for most values of E there are no corresponding normalizable wavefunctions. This energy quantization is a consequence of the normalization condition. The values of the energy for which there is a corresponding wavefunction are labeled by quantum numbers.

Figure 2 shows another potential energy surface. Wavefunctions in the well region below E_1 have discrete, quantized energies. Above E_1 , however, normalizable wavefunctions exist for all energies. We see in Section IV that molecules are bound to metal surfaces by interactions similar to that sketched in Figure 2.

I. C. The hydrogen atom

Study of the hydrogen atom was very important for the development of quantum mechanics because there was no classical explanation for the observed spectrum. It is still studied because it is relatively simple, and has exact analytic solutions. Furthermore, we will see that many other atoms (such as the alkali metals) have electronic levels similar to hydrogen.

The potential energy describing the interaction of the hydrogen nucleus (a proton) with an electron is:

$$U(r) = -\frac{1}{4\pi\epsilon_0} \frac{e^2}{r} \quad (14)$$

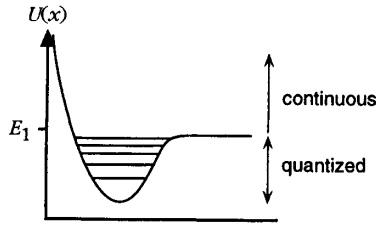


Figure 2 A potential energy surface with a region in which the energies are quantized (the bound-state well), and a region in which all energies are permitted. After [2].

where r is the radial distance from the nucleus to the electron. This potential produces a bounded well: we therefore expect quantized energies. Solution of the Schrödinger equation confirms that the energy of the electron depends on the quantum number n according to:

$$E_n = -E_I \frac{1}{n^2}. \quad (15)$$

The energy is defined in terms of the ionization energy, $E_I \approx 13.6$ eV. The energies of the electronic states of hydrogen are plotted in Figure 3.

The solutions of the Schrödinger equation for potential energy (14) and total energy (15) factor into radial and angular terms:

$$\Psi(r, \theta, \phi) = R_{n,l}(r) Y_{l,m}(\theta, \phi). \quad (16)$$

The angular dependence is entirely in the term $Y_{l,m}(\theta, \phi)$, called a spherical harmonic.[3] The radial dependence is contained in $R_{n,l}(r)$, [3] plotted in the left side of Figure 4 for various values of $n = 0, 1$, or 2 . The radial distributions are usually expressed in terms of length scale

$$a = \frac{4\pi\epsilon_0\hbar^2}{m_e e^2} \approx 0.54 \text{ \AA}, \quad (17)$$

known as the Bohr radius.

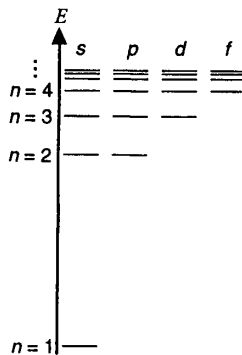


Figure 3 Energy levels of the hydrogen atom. The energies are independent of the values of l (s, p, d, \dots). Each state may contain two electrons of opposite spin.

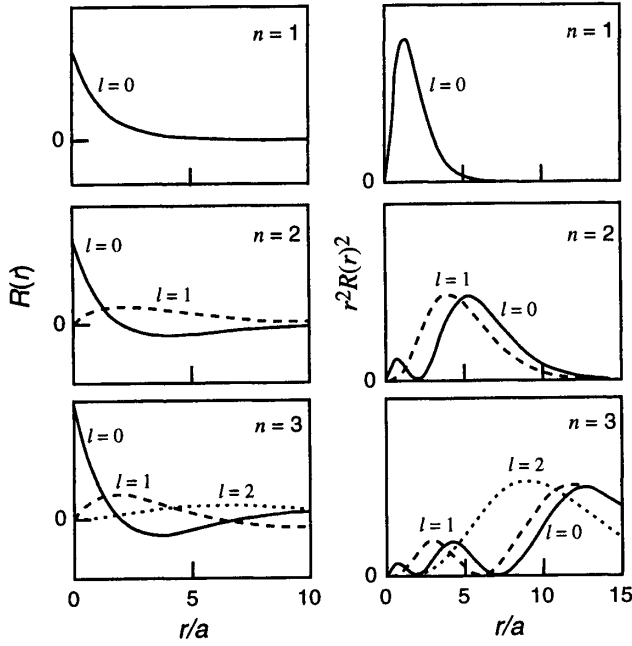


Figure 4 Radial dependence of the wavefunctions of the hydrogen atom (left). The $l = 0$ wavefunctions (the s -waves) are nonzero at the nucleus. The probability of finding the electron at radius r/a scales as $r^2 R^2$ (right). The length scale a is the Bohr radius. After [2].

The values of the quantum number l in Equation 16 are integers in the range $0 \dots (n - 1)$. The values of l are represented with letters; s for $l = 0$, p for $l = 1$, d for $l = 2$, f for $l = 3$, with g and subsequent letters used for the higher values of l . The parameter m is called the magnetic quantum number. The values of m lie in the range $-l < m < l$.

The probability of finding the electron at radius r from the nucleus scales as $r^2 R_{n,l}(r)^2 dr$. The right side of Figure 4 shows how $r^2 R^2$ depends on r . When $n = 1$, the electron is most likely found near $r/a = 1$, the Bohr radius. For $n = 2$ the radial distribution depends on l : the $l = 0$ probability distribution has a lobe which is closer to the nucleus than $l = 1$. A similar trend occurs for $n = 3$ where again the probability of finding the electron near the nucleus is greatest for lowest values of l .

According to Equation 15 and Figure 3, the energies of the electronic states of hydrogen do not depend on l . We will see below that in multi-electron atoms the energies of the states depend on l and their relative energies can be predicted from the spatial distributions of the wavefunctions.

It is possible to show using symmetry (and other) arguments that optical transitions between states of the hydrogen atom are constrained to satisfy selection rules. For example, a transition induced by an electric dipole interaction[3] between the atom and an external electric field must satisfy $\Delta l = \pm 1$. Transitions from s to p are allowed, but s to d is forbidden. Restrictions on Δm depend on the polarization of the light. There is no restriction on Δn . [2]

Figure 3 does not tell the whole story because it fails to represent the fine structure. The fine structure is a deviation of the electronic levels sketched in Figure 3 on a scale of about

10^4 times smaller than the ionization energy. Fine structure arises from several different interactions, including relativistic effects due to the high speed of the electron, effects related to the nonlocal distribution of the electron's wavefunction, and an interaction between the magnetic moment due to orbital motion of the electron around the nucleus with the magnetic moment associated with the spin of the electron. This last interaction is called spin-orbit coupling. When the magnetic moments of orbital and spin origin are parallel, the interaction energy is higher than when they are antiparallel. This energy difference is the spin-orbit coupling.[3]

A consequence of the spin-orbit coupling is that neither the orbital angular momentum (\vec{l}) nor the spin angular momentum (\vec{s}) is constant. (In quantum mechanical language we say that neither operator commutes with the Hamiltonian.) The sum, \vec{j} , however, is constant and has two possible magnitudes depending on the relative orientations of \vec{l} and \vec{s} . Each value of $|\vec{j}|$ is called a level. For example, if $l = 2$, two levels are possible:

$$|\vec{j}| = |\vec{l} + \vec{s}| = 3/2 \text{ or } 1/2. \quad (18)$$

Each level has a different energy. The actual spectrum of hydrogen is also influenced by other contributions to the fine structure (listed above) which have effects on the same scale as the spin-orbit coupling.

There is also a hyperfine structure which is due to the spin of the proton. (The proton, like the electron, is a spin 1/2 particle.) One of the ways it influences the electronic levels is by interacting with the magnetic field caused by the motion of the electron. Hyperfine interactions are on the order of 10^3 times smaller than fine-structure interactions.[3]

I. D. Multi-electron atoms

It is not possible to find exact solutions for the energies and wavefunctions of atoms with two or more electrons. Interactions between electrons complicate the expression for the potential energy of any one electron. An approximate solution is obtained by considering one electron at a time and accounting for only an average interaction with the other electrons. The other electrons are pictured as forming a cloud around the nucleus. From outside the cloud, the rest of the atom appears to be a single positive charge because attraction to the Z charges in the nucleus (where Z is the atomic number) is partially offset by repulsion from $Z - 1$ electrons in the cloud. The effective potential outside the cloud varies as

$$V_{eff}(r) \sim \frac{e^2}{r}. \quad (19)$$

The electron outside the cloud is shielded from most of the nuclear charge. When the electron penetrates the cloud, however, it interacts with all of the nuclear charge, Ze , without shielding from the cloud. In this case the effective potential varies as

$$V_{eff}(r) \sim \frac{Ze^2}{r}. \quad (20)$$

According to Equations 19 and 20, electrons with wavefunctions that extend to the core experience a larger attraction to the nucleus and have a lower (more negative) energy than orbitals that do not extend inside the cloud.

Figure 5 shows two hydrogen atom wavefunctions. For fixed n , wavefunctions with low l penetrate towards the nucleus more than wavefunctions with higher l . The low l wavefunctions

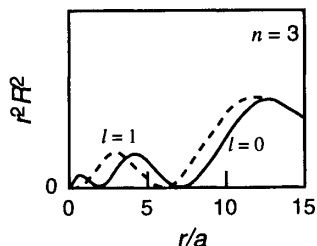


Figure 5 The $l = 0$ (s -orbital, bold) state extends closer to the nucleus ($r = 0$) than the $l = 1$ (p -orbital). When additional electrons form a shell around the nucleus, the penetration of the s -orbital towards the nucleus causes it to have lower energy than the p -orbital.

interact more with the core than the high l wavefunctions. Consequently, in a multi-electron atom, the $n = 3, l = 0$ energy, for example, is below the $n = 3, l = 1$ energy. The influence of the electron cloud is essential to this argument; in the single-electron atom the energy is independent of l .

The energy level diagrams for hydrogen, lithium, and sodium are indicated below. In lithium the shielding of the core causes the s, p , and d energies to be different. In sodium the difference is so great that the $3d$ orbital is higher in energy than the $4s$ orbital.

Shielding is particularly effective for alkali metals such as lithium, sodium, and potassium. Their outermost electron lies at a higher value of n than the rest of the electrons in the atom. The lower-lying electrons form a closed shell, which means that they occupy all states of lower n . A similar situation occurs for noble metals, such as copper, silver, and gold. These metals have a single electron in an s -orbital and 10 electrons in (fully occupied) d -orbitals. The fully-occupied d -orbitals tend to shield the outermost electron from the nucleus. The alkali metals and the noble metals are together called monovalent metals because they both have a single electron outside a shielded nucleus. Electrons that lie outside the closed shell are called valence electrons.

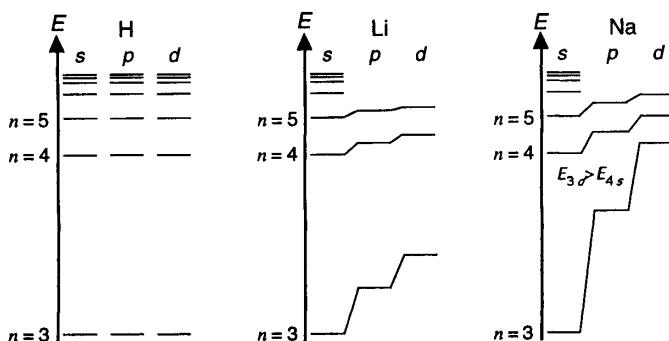


Figure 6 Energy level diagrams for the first few alkali metals. In hydrogen, the energy levels are independent of l . In atoms with closed shells, states of high l have relatively high energy compared with states of lower l and the same n . In sodium this effect is large enough that the energy of the $3d$ state is higher than the energy of the $4s$ state.

The approximate electronic state of an atom is stated by specifying its configuration. Configuration is represented by nl^i where i is the number of electrons occupying the orbital with the values n and l . For example, $1s$ and $1s^2$ refer to configurations in which the $n = 1, l = 0$ orbital is singly ($1s$, as in ground state hydrogen) or doubly ($1s^2$, as in ground state helium) occupied. Excited state configurations may be represented with this notation: the configuration of ground state oxygen, $1s^2 2s^2 2p^4$, becomes $1s^2 2s^2 2p^3 3s$ following excitation of an electron to $3s$. Each s -orbital ($l = 0$) may contain two electrons corresponding to the two spin states, and each p -orbital ($l = 1$) may contain six electrons corresponding to two electrons in each of the $m = -1, 0, 1$ states. The configuration only approximately gives the electronic state of the atom because the notation does not account for details in the electronic levels arising from the interactions between electrons in the atom. A more complete notation is described after a brief discussion of the helium atom.

I. E. Helium atom

The simplest atom in which there are electron-electron interactions is helium. Helium is not well described as a single electron bound to a nucleus with a screening cloud (as alkali metals are described) because both electrons occupy the same orbital. The energy of each electron is raised by Coulomb interactions with the other electron. Another complication is exchange interaction which is a purely quantum mechanical contribution to the energy. It arises from the laws of quantum mechanics applied to two indistinguishable objects. According to a law of quantum mechanics, if the electrons in a two-electron wavefunction are exchanged, there can be no change in the probability distribution, $|\Psi|^2$. For example, the wavefunctions representing one electron in an s -orbital and another in a p -orbital

$$\Psi_T = \Psi_s(1)\Psi_p(2) \text{ or, } \Psi_T = \Psi_p(1)\Psi_s(2), \quad (21)$$

have different values of $|\Psi|^2$, even though the only difference between them is an exchange of the roles of electrons labeled 1 and 2. Wavefunctions which are invariant under exchange of the electrons may be constructed as follows:

$$\Psi_{\pm} = \frac{1}{\sqrt{2}} [\Psi_s(1)\Psi_p(2) \pm \Psi_p(1)\Psi_s(2)]. \quad (22)$$

If the indices 1 and 2 are exchanged, representing exchange of the two electrons, the value of $|\Psi|^2$ is unchanged. The wavefunctions Ψ_+ and Ψ_- have different energies. The energy difference is called exchange splitting.

In classical mechanics, if two interacting bodies move under the influence of a central potential (such as two planets orbiting a sun) the total angular momentum of the two bodies is conserved. However, their mutual interaction exchanges angular momentum between them so that the angular momentum of either body alone is not conserved. Similarly, in the quantum mechanical description of an atom with two electrons, the angular momentum of a single electron, \bar{l}_1 or \bar{l}_2 is not constant, but the total orbital angular momentum,

$$\bar{L} = \bar{l}_1 + \bar{l}_2, \quad (23)$$

is constant. The quantum numbers corresponding to \bar{L} are represented by the capital letters S, P, D , etc. The total spin angular momentum,

$$\bar{S} = \bar{s}_1 + \bar{s}_2, \quad (24)$$

$$2S+1 \{L\}_J$$

Figure 7 Standard atomic spectroscopy notation. The spectral term is represented inside the brackets with a letter. The level is specified in the lower right corner. $2S + 1$ in the upper left specifies the multiplicity of the electronic spin states.

may be either 0 or 1, depending on whether the spins of the electrons are parallel or anti-parallel. The values of L and S determine a spectral term.

If there were no interactions between the orbital angular momentum, \vec{L} , and the spin angular momentum, \vec{S} , then (23) and (24) would be good operators to describe the atom. However, as in the hydrogen atom, there are fine structure interactions which couple the angular and spin momenta. The total angular momentum

$$\vec{J} = \vec{L} + \vec{S}, \quad (25)$$

is conserved with fine structure interactions. There are $2S + 1$ possible values for J which together are called a multiplet. The quantity $2S + 1$ is called the multiplicity of the state. For example, when $S = 0$ there is one possible value for \vec{J} , determined by \vec{L} . When $S = 1$, the multiplicity is three. The $S = 0$ state is called a singlet, and the $S = 1$ state is called a triplet. A particular value of J determines the level. Figure 7 shows the standard spectroscopic notation. It specifies the term, the level, and the multiplicity of the atom. For example, the electronic ground state of helium is represented as 1S_0 .

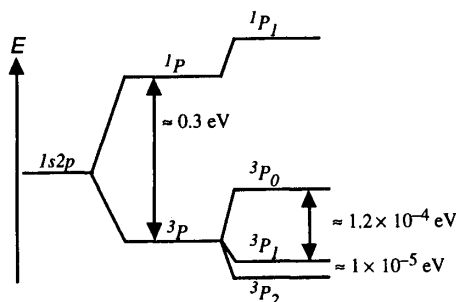


Figure 8 The energy level diagram for a two electron atom. Electrons in the $1s$ and $2p$ orbitals combine with total angular momentum $L = 1$, a P -state. Two possible terms are represented, corresponding to the two ways the spin angular momenta may combine: $S = 0$ or $S = 1$. Their energies are different because of exchange splitting. Fine-structure interactions cause the terms to split into levels corresponding to the $2S + 1$ possible values of J . After [3].

Figure 8 represents the energies of the possible levels in the $1s2p$ configuration. The energy difference between the levels has been exaggerated. Figure 8 does not tell the whole story. As in the hydrogen atom, an additional hyperfine splitting further complicates atomic spectra. Hyperfine splitting is described in many text books.[3]

I. F. Chemical bonds

When atoms are close together, the electrons from different atoms interact and may form chemical bonds. Attraction between the atoms causes the atoms in a molecule (or solid) to have lower total energy than separate atoms. At close range the atoms repel each other, preventing the molecule from collapsing. A potential energy surface which represents these qualitative features of the interaction is sketched in Figure 9.

The total energy of the molecule depends on the motion of the nuclei such as vibrations or rotations of the molecule and translation of the center of mass. While considering the internal excitation of the molecule, we typically ignore the translational energy. The various internal excitations evolve on very different timescales. Electronic motion occurs at about 10^{15} Hz. Vibrations occur at about 10^{13} Hz. Rotational motion is slower still at 10^7 – 10^{11} Hz. The electronic part of the Schrödinger equation may be solved while assuming the nuclei are at fixed locations because the electronic motion occurs so much more quickly than the nuclear motions. With this Born-Oppenheimer approximation we write the wavefunction as a separable function:

$$\Psi \approx \Psi_e(\vec{r}_e, \vec{R}_N) \chi_N(\vec{R}_N) \approx \Psi_e \Psi_v \Psi_R. \quad (26)$$

Here the nuclear wavefunction χ_N is written as a product of vibrational, Ψ_v , and rotational, Ψ_R , components.

The strongest bond is the covalent bond, which is formed by an overlap of charge distribution between neighboring atoms. The lowering of the total energy comes about because electrons are shared between nuclei. Figure 10 schematically illustrates covalent bonding between two atoms. If the two atoms get close enough for the atomic orbitals to overlap, then the wavefunctions of these orbitals can add with either the same or opposite phase. The two new orbitals have different energies. The lower level corresponds to the wavefunctions adding in phase while the upper level corresponds to adding with opposite phase. Electrons which occupy the symmetric state are concentrated primarily in between the two nuclei; they draw both nuclei towards the center by coulomb attraction to the positive charges on the nuclei. They are known as bonding orbitals. The electrons in the anti-symmetric wavefunctions, however, have a low probability of being between the nuclei. Electrons in these states tend to pull the molecule apart, and are called anti-bonding. If both of the original electronic levels in each atom were singly occupied, then in the ground state of the new system, the two electrons occupy the bonding orbital. Since this state is energetically

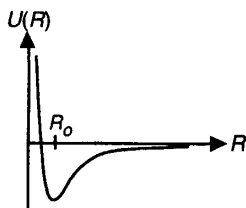


Figure 9 The qualitative form of the interaction potential between two nuclei in a diatomic molecule. The potential energy is plotted against the separation of the nuclei. The equilibrium separation of the nuclei is R_0 .

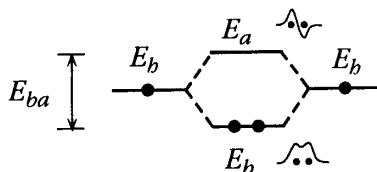


Figure 10 Energy level splitting in a covalent bond between two atoms.

more favorable than the state in which the two atoms are separated, the sharing of the two electrons results in a bond between the two atoms. In the case of a solid consisting of many atoms, the bonding and antibonding levels broaden into bands. We return to the topic of bands below.

The wavefunctions sketched in Figure 10 represent the combination of two s -orbitals. In general, the combination of the orbitals is more complicated. If the combined orbital is symmetric under rotation about the nuclear axis then the resulting bond is called a σ -bond.

The bonding of two atoms is determined by the balance between the electrons in bonding orbitals, and electrons in anti-bonding orbitals. For example, two hydrogen atoms (each in a ground-state $1s^1$ configuration) make H_2 because each atom contributes one electron to a σ bonding orbital. The orbital may contain two electrons without violating the Pauli exclusion principle because there are two available spins for each electron. Two He atoms, however, do not form a bond because the initial $1s^2$ configuration of each atom would result in a molecule with two electrons in a bonding orbital, and two electrons in an anti-bonding orbital, for no net bonding.

The formation of diatomic oxygen, O_2 , is more complicated because each atom has 4 valence electrons. Three electrons from each atom go into bonding orbitals: 2 in each of two π orbitals, and 2 in the σ orbital. The remaining two electrons go into anti-bonding π^* orbitals. Overall there are 4 more electrons in bonding orbitals than anti-bonding. A full bond is formed when two electrons occupy a bonding orbital. Molecular oxygen has four such electrons, so O_2 has a double bond.

I. G. Vibrations of diatomic molecules

We now consider the vibrational motion of the nuclei in a diatomic molecule. Figure 9 qualitatively illustrates the interaction between two atoms comprising a molecule. The equilibrium separation of the atoms is R_o . The vibrations are usually small with respect to the internuclear separation, R . Writing the potential as a Taylor series expansion about the equilibrium position R_o in terms of $Q \equiv R - R_o$, we have

$$U(Q) = U(0) + \left(\frac{dU}{dQ} \right)_o Q + \frac{1}{2} \left(\frac{d^2U}{dQ^2} \right)_o Q^2 + \text{anharmonic terms} \quad (27)$$

The anharmonic terms contain additional nonvanishing derivatives of $U(Q)$. The first derivative of $U(Q)$ is zero at R_o . Neglecting anharmonic contributions, the potential is quadratic in Q :

$$U(Q) \approx \frac{1}{2} k Q^2, \quad k = \left(\frac{d^2U}{dQ^2} \right)_o \quad (28)$$

In classical mechanics, two atoms of mass m_a and m_b interacting with this potential vibrate sinusoidally at frequency

$$\omega = (k/\mu)^{1/2} \quad (29)$$

where μ is the reduced mass:

$$\frac{1}{\mu} \equiv \frac{1}{m_a} + \frac{1}{m_b}. \quad (30)$$

The Schrödinger equation describes the wavefunction for two particles interacting by the quadratic potential in Equation 28.

$$\nabla^2 \Psi + \frac{2m}{\hbar} \left[E - \frac{1}{2} k Q^2 \right] \Psi = 0 \quad (31)$$

The solution is an energy spectrum with equally-spaced energy levels:

$$E_v = \left(v + \frac{1}{2} \right) \hbar \omega, \quad v = 0, 1, 2, \dots \quad (32)$$

The wavefunctions are sketched in Figure 11. In the ground state the nuclei are most likely to be found at separation $Q=0$, *i.e.*, at their equilibrium separation, $R=R_0$. At higher levels of excitation the nuclei are most likely to be found at the limits of their oscillation (largest and smallest R). In classical mechanics a simple harmonic oscillator spends most of its time at the positions of greatest displacement where the velocity is lowest. The similarity of the quantum mechanical and classical behaviors for high quantum numbers is known as the correspondence principle.

The harmonic approximation is a good representation of the interaction potential at low levels of excitation where the Taylor series (27) remains a good approximation to the actual interaction potential. The harmonic approximation is particularly valuable because it has an exact solution.

Another expression for the interaction potential which has an exact solution is the Morse potential[4]:

$$U(Q) = D_e \left(1 - e^{-\alpha Q} \right)^2. \quad (33)$$

This is the function sketched in Figure 9; it increases rapidly at small separation and

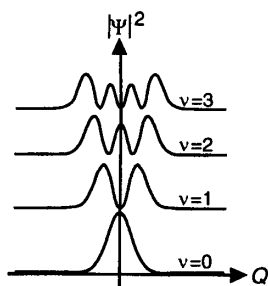


Figure 11 Squares of the wavefunctions of the harmonic oscillator (offset for clarity). At successively higher vibrational excitations (higher v), the nuclei are more and more likely to be found at large separation, in agreement with a classical harmonic oscillator.

disappears at large separation. The energies of the bound states in a Morse potential are

$$E_v = \left(v + \frac{1}{2} \right) \hbar \omega - \left(v + \frac{1}{2} \right)^2 \hbar \omega x. \quad (34)$$

The constant x depends on D_e and α . The second term is a correction to the energy of a harmonic oscillator (32). We stress that Equations 32 and 34 are just the energies of states of the artificial potential energy surfaces (28, 33) used in these calculations. Real molecular spectra depend on the actual interaction potential between the atoms.

I. H. Electronic transitions in diatomic molecules

Electronic transitions are often depicted in potential energy *versus* nuclear separation diagrams such as Figure 12. The Figure shows an electronic ground state potential energy surface, **X**, and the potential energy surface corresponding to an excited electronic state, **A**. In this example, the excited state **A** has a minimum at larger R than the ground state. An arrow represents a transition from **X** \rightarrow **A**. The transition is vertical in this diagram because electronic transitions occur much faster than nuclear motion, R .

The most probable transitions are between vibrational states with probability maxima at the same R . This is called the Frank-Condon principle. At high levels of vibrational excitation, the molecule is most likely to be found towards the limits of the oscillation, while in the ground state the probability distribution is concentrated near $R = R_0$ (Figure 11). The vertical transition in Figure 12 satisfies the Frank-Condon principle because it is a transition from the equilibrium position in the ground state to an extreme limit of motion in an excited (vibrational) state.

Spectra of molecules are further complicated by rotational excitations. Transitions between rotational states lie in the microwave region of the spectrum; transitions between vibrational states lie in the infrared region of the spectrum, and electronic transitions span the range from infrared through visible to the ultraviolet.

Additional details to this brief introduction are provided below as some of the concepts are applied to the study of chemical reaction of adsorbates at metal surfaces.

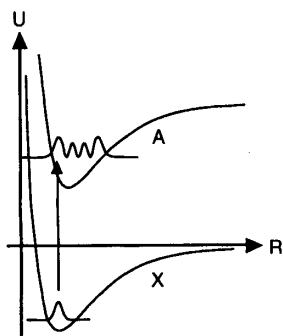


Figure 12 A transition between the electronic ground state of a molecule, **X**, and an excited electronic state, **A**. The displacement of these (hypothetical) potential energy surfaces ensures that the ground state wavefunction overlaps well with an excited vibrational state wavefunction. The transition shown satisfies the Frank-Condon principle.

II. OPTICAL PROPERTIES OF SOLIDS

Here we introduce some of the concepts that are relevant to understanding how light interacts with solids. A simple and very powerful model for the behavior of electrons in a solid is introduced, elucidating many optical properties of materials.

II. A. Propagation of electromagnetic waves in vacuum

In vacuum the frequency f and the wavelength λ of an electromagnetic wave are related by the speed c of light in vacuum,

$$f\lambda = c. \quad (35)$$

This yields a linear relation between the angular frequency $\omega \equiv 2\pi f$ and the wavevector $k \equiv 2\pi/\lambda$:

$$\omega = ck. \quad (36)$$

In a medium, the propagation of an electromagnetic wave is determined by the response of the material to electric and magnetic fields and is characterized by the dielectric constant ϵ , the magnetic permeability μ , and the electric conductivity σ . Except for the magnetic permeability, which is nearly frequency independent at optical frequencies, the response of the medium depends on the frequency of the incident wave, and so dispersion occurs: waves of different frequencies propagate at different speeds. The frequency-dependent speed v of light in a medium is given by

$$v = \frac{c}{\text{Re}\sqrt{\epsilon(\omega)}} \equiv \frac{c}{n(\omega)}, \quad (37)$$

where $\epsilon(\omega)$ is the frequency-dependent dielectric function and $n(\omega)$ the index of refraction of the medium. This frequency dependence results in a nonlinear relation between the angular frequency and the wavevector of the electromagnetic wave:

$$\omega = \frac{c}{\text{Re}\sqrt{\epsilon(\omega)}} k. \quad (38)$$

Equation 38 is an example of a dispersion relation. It relates photon energy $E = \hbar\omega$ to wavevector. Figure 13 shows the dispersion relations, and the relationships between dielectric function and angular frequency, in vacuum and in a medium. Throughout this part of the lectures we use similar graphs to represent the optical properties of materials. The questions addressed are: why do different materials have different optical and electronic properties and what fundamental properties of solids are responsible for this behavior?

II. B. Propagation of electromagnetic waves through a medium

The electromagnetic response of a material varies over the frequency spectrum because the charges present in the material respond at widely different frequencies. Roughly speaking, we can subdivide the charges into the following categories: ionic cores (the nuclei and core electrons at each lattice site), valence electrons, and free electrons. The ionic cores can form dipoles that tend to orient themselves along the direction of the applied external fields. This motion is usually limited to low frequencies and therefore only contributes to the polarization — and hence the propagation of the wave — at frequencies in the microwave region and below (see Figure 14). At higher frequencies the dipoles can no longer follow the rapid

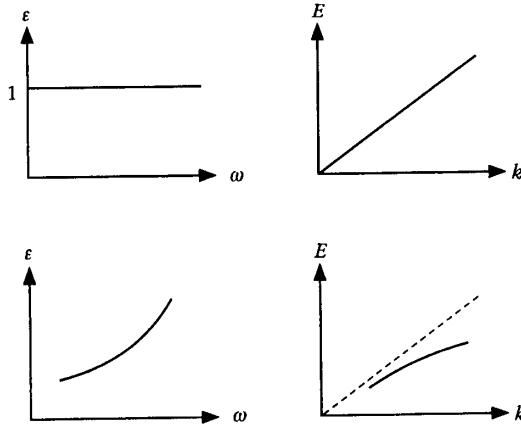


Figure 13 Dielectric function and energy-wavevector relationships in vacuum (top) and in a medium (bottom).

oscillation of the applied field and their contribution to the dielectric constant vanishes. Lattice vibrations (displacement of the ionic cores) induced by the applied field contribute at frequencies up to the infrared region of the electromagnetic spectrum. In the visible and ultraviolet regions only the response of the free and bound valence electrons remain. Core electrons contribute at high frequency (10–1000 eV), but unless absorptions occur their contributions to the polarizability are generally small and therefore the dielectric constant is close to 1 for x-rays. The dielectric function in Figure 14 is very schematic — real materials generally show more structure and, depending on the type and number of charges present, some of the features shown may not be there.

Let us begin by analyzing the motion of a bound valence electron in response to an external driving field. If the field oscillates at frequency ω , the electron oscillates at the same frequency with the phase and the amplitude of the oscillation determined by the binding and damping forces on the electron. The oscillation is described by the equation of motion of the electron:[5]

$$m \frac{d^2 x}{dt^2} = -m\omega_0^2 x - m\gamma \frac{dx}{dt} - eE. \quad (39)$$

The first term on the right hand side of the equation represents a binding force with spring constant $k = m\omega_0^2$, where m and ω_0 are the mass and the resonant frequency of the bound electron, respectively. The second term is a velocity-dependent damping force and the third term is the driving force with E the applied field. Rearranging terms and assuming a sinusoidally varying applied field of amplitude E_0 and frequency ω , we obtain an inhomogeneous second-order differential equation

$$m \frac{d^2 x}{dt^2} + m\gamma \frac{dx}{dt} + m\omega_0^2 x = -eE_0 e^{-i\omega t}. \quad (40)$$

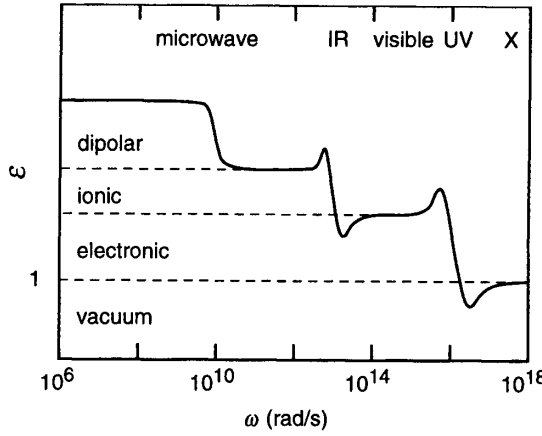


Figure 14 Schematic illustration of the various contributions to the dielectric constant across the electromagnetic spectrum.

The steady-state solution of this equation, representing the oscillating motion of the electron, must be of the form

$$x(t) = x_0 e^{-i\omega t} \quad (41)$$

Substituting this into Equation 40, we get for the amplitude of the motion

$$x_0 = -\frac{e}{m} \frac{1}{(\omega_0^2 - \omega^2) - i\gamma\omega} E_0 \quad (42)$$

As is to be expected, the amplitude of the electrons is maximal when the driving frequency is equal to the resonance frequency. The motion of the electron results in an oscillating dipole moment

$$p(t) = -ex(t) = \left(\frac{e^2}{m} \right) \frac{1}{(\omega_0^2 - \omega^2) - i\gamma\omega} E_0 e^{-i\omega t} \quad (43)$$

In a sample with many bound electrons, the dipole moments of all the electrons contribute to a polarization

$$P(t) = \left(\frac{Ne^2}{m} \right) \sum_j \frac{f_j}{(\omega_j^2 - \omega^2) - i\gamma_j\omega} E_0 e^{-i\omega t} \quad (44)$$

where N is the total number of electrons, and f_j is the fraction of electrons having a resonant frequency ω_j and damping constant γ_j . In quantum mechanical terms, the factor Nf_j is the oscillator strength. This factor indicates how much each resonance contributes to the polarization.

The relation between the polarization P and the electric field E is usually written as $P(t) = \epsilon_0 \chi_e E(t)$, with χ_e the dielectric susceptibility, and $E(t) = E_0 e^{-i\omega t}$. The dielectric constant is given by $\epsilon(\omega) = 1 + \chi_e$, so that

$$\epsilon(\omega) = 1 + \frac{Ne^2}{\epsilon_0 m} \sum_j \frac{f_j}{(\omega_j^2 - \omega^2) - i\gamma_j\omega} = \epsilon'(\omega) + i\epsilon''(\omega) \quad (45)$$

Figure 15 shows the frequency dependence of the dielectric constant for a single resonance and the resulting $E(k)$ -behavior. At resonance, dissipation of energy is maximized since the amplitude of the electron motion is maximized. This dissipation of electromagnetic energy is what we call absorption and is reflected by the peak in the imaginary part of the dielectric constant at the resonance frequency. Note, also, that the real part crosses through zero near the resonance.

Let us next turn to the response of free electrons to an oscillating electromagnetic wave. Setting the binding force in Equation 40 to zero we get

$$m \frac{d^2 x}{dt^2} + m\gamma \frac{dx}{dt} = -eE_0 e^{-i\omega t}. \quad (46)$$

Again, we obtain a solution of oscillating form,

$$x(t) = \frac{e}{m} \frac{1}{\omega^2 + i\gamma\omega} E_0 e^{-i\omega t}, \quad (47)$$

but because there is no binding term, the motion does not exhibit any resonances. At low frequency, $\omega/\gamma \ll 1$, the applied electric field induces a time-varying current

$$J(t) \equiv \frac{dq}{dt} = -Ne \frac{dx}{dt} = \frac{Ne^2}{m} \frac{1}{\gamma - i\omega} E(t) \approx \frac{Ne^2}{m\gamma} E(t) \equiv \sigma E(t), \quad (48)$$

where N is the number of free electrons and σ the conductivity.

At high frequency the current can no longer keep up with the driving field and we may no longer ignore the imaginary part of the conductivity. Let us therefore again consider the oscillating dipole moment created by each electron:

$$p(t) = -ex(t) = -\left(\frac{e^2}{m}\right) \frac{1}{\omega^2 + i\gamma\omega} E_0 e^{-i\omega t}. \quad (49)$$

For a sample with N free electrons, the polarization is

$$P(t) = -\left(\frac{Ne^2}{m}\right) \frac{1}{\omega^2 + i\gamma\omega} E(t) \equiv \epsilon_0 \chi_e E(t). \quad (50)$$

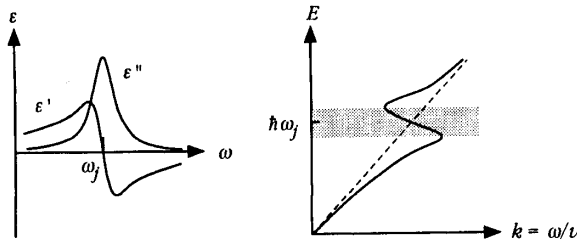


Figure 15 Frequency dependence of the dielectric function near a resonance (left) and the resulting relation between energy and wavevector (right). The shaded region indicates the range of values for which electromagnetic waves are strongly attenuated and do not propagate.

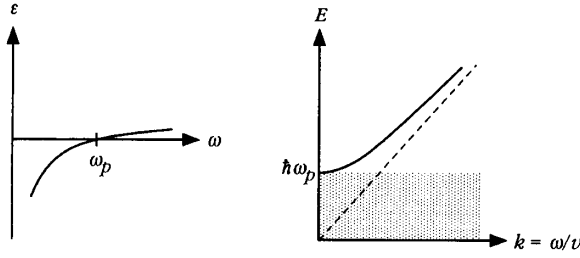


Figure 16 Dielectric function and $E(k)$ behavior for a plasma of free electrons with zero damping. The shaded region corresponds to a forbidden band of frequencies. Electromagnetic waves within this region are strongly attenuated.

From this expression we obtain the free-electron contribution to the dielectric constant:

$$\varepsilon(\omega) = 1 - \left(\frac{Ne^2}{m\varepsilon_0} \right) \frac{1}{\omega^2 + i\gamma\omega} = \varepsilon'(\omega) + i\varepsilon''(\omega). \quad (51)$$

If the damping is negligible, $\gamma \ll \omega$, the imaginary part of the free-electron contribution vanishes, and the real part becomes

$$\varepsilon'(\omega) = 1 - \frac{Ne^2}{m\varepsilon_0} \frac{1}{\omega^2} \equiv 1 - \frac{\omega_p^2}{\omega^2}, \quad (52)$$

where ω_p is called the plasma frequency. For frequencies below the plasma frequency, the dielectric constant is negative and so the index of refraction is purely imaginary resulting in strong attenuation of the electromagnetic wave (see Figure 16). In the $E(k)$ -plot this attenuation gives rise to a range of 'forbidden frequencies', or frequency gap below the plasma frequency. In this regime, however, the reflectivity is nearly one and incident electromagnetic waves do not penetrate into the plasma. Above the frequency gap the electromagnetic wave propagates through the medium and at high frequency the dielectric function approaches unity. The free electrons thus act like a high-pass filter: below the plasma frequency reflection occurs; above the plasma frequency the free electrons are transparent. For intrinsic semiconductors, the plasma frequency lies in the microwave or infrared part of the electromagnetic spectrum. Metals reflect visible light because their plasma frequency is higher than visible optical frequencies.

The effect of small, but nonzero damping is illustrated in Figure 17. The damping results in a nonzero imaginary part at low frequency and a reduction of the frequency gap in the $E(k)$ -plot. At high frequency the real part still approaches unity and the imaginary part vanishes.

II. C. Nonlinear optical interactions

Next we consider the nonlinear optical properties of materials. In the presence of an electric field $E(t)$, atoms in a solid become polarized giving rise to a polarization of the solid. For small electric fields, the induced polarization is linear in the applied field:

$$P(t) = \chi^{(1)} E(t), \quad (53)$$

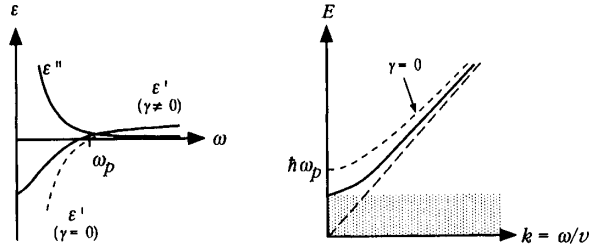


Figure 17 Dielectric function and $E(k)$ behavior for a plasma of free electrons with small nonzero damping. Damping reduces the forbidden band of frequencies.

with $\chi^{(1)}$ the linear susceptibility. For large applied fields, however, the induced polarization becomes nonlinear in the applied field[6]:

$$\begin{aligned} P(t) &= \chi^{(1)} E(t) + \chi^{(2)} E^2(t) + \chi^{(3)} E^3(t) + \dots \\ &= P^{(1)}(t) + P^{(2)}(t) + P^{(3)}(t) + \dots \end{aligned} \quad (54)$$

The first term represents the linear polarization, $P^{(n)}$ the n -th order polarization, and $\chi^{(n)}$ the n -th order nonlinear optical susceptibility. In general, the n -th order nonlinear susceptibility is not a scalar, but a tensor of rank $(n + 1)$. For typical materials the electric field has to be of the order of atomic field strengths E_{at} before the second-order term becomes comparable to the linear term:

$$\chi^{(n)} \approx \frac{\chi^{(1)}}{E_{at}^{n-1}}. \quad (55)$$

The nonlinear polarization can drive a new field. According to the wave equation that follows from the Maxwell equations, we have[6]

$$\nabla^2 E - \frac{n^2}{c^2} \frac{\partial^2 E}{\partial t^2} = \frac{4\pi}{c^2} \frac{\partial^2 P^{NL}}{\partial t^2}. \quad (56)$$

The second-order polarization, for instance, causes a driving term proportional to the square of the applied electric field, resulting in a new field at twice the applied frequency.

Consider an electron in the interstitial region between four atoms, as shown in Figure 18a. Physically, the doubling of the frequency comes about because the charges move along a curved potential plane. For an electric field oscillating in the plane of the drawing, the electron moves along the dotted arc; in addition to being displaced in the horizontal direction, the electron also undergoes a small vertical displacement. This vertical displacement gives rise to a small second-order dipole moment perpendicular to the horizontal first-order dipole moment. As Figure 18b shows, the period of oscillation of the second-order dipole moment is half that of the first-order dipole moment.

For systems with inversion symmetry, however, the second-order susceptibility vanishes. This can readily be seen by writing the second term of Equation 54 in tensorial form:

$$\mathbf{P}^{(2)} = \chi^{(2)} : \mathbf{E}\mathbf{E}. \quad (57)$$

Applying inversion, we get

$$-\mathbf{P}^{(2)} = \chi^{(2)} : (-\mathbf{E})(-\mathbf{E}), \quad (58)$$

and from Equations 57 and 58 we see that $\chi^{(2)} = -\chi^{(2)}$, which can only be satisfied if $\chi^{(2)} = 0$.

For systems that do not have inversion symmetry, $\chi^{(2)}$ is not zero and an intense field causes a second-order polarization. Let the applied field be of the form

$$E(t) = \frac{1}{2} E e^{i\omega t} + \text{c.c.} \tag{59}$$

The second-order polarization is then

$$P^{(2)} = \chi^{(2)} E^2(t) = \frac{1}{2} \chi^{(2)} E E^* + \frac{1}{4} \left\{ \chi^{(2)} E^2 e^{-i2\omega t} + \text{c.c.} \right\}. \tag{60}$$

The second term on the right-hand side oscillates at frequency 2ω and can drive a new electromagnetic wave at double the incident frequency. This process is called second-harmonic generation.

If two oscillating fields of different frequency are present,

$$E(t) = \frac{1}{2} E_1 e^{i\omega_1 t} + \frac{1}{2} E_2 e^{i\omega_2 t} + \text{c.c.}, \tag{61}$$

the second-order polarization contains terms at frequencies $2\omega_1$, $2\omega_2$, at the sum-frequency $\omega_1 + \omega_2$, at the difference frequency $\omega_1 - \omega_2$, and at zero frequency. Because of dispersion, the output beam at these new frequencies and the input beams at ω_1 and ω_2 travel at different velocities. To maximize output at any of the new frequencies it is therefore necessary to geometrically match the phases of the input and output beams.[6]

Let us next briefly turn to the third-order polarization which ‘mixes’ four electric fields — three input fields generate one new output field. When three different input frequencies are present, 13 new frequencies can be generated. An example of a third-order effect is coherent anti-Stokes Raman spectroscopy (CARS). Two of the input frequencies are chosen such that their difference matches a resonant frequency in the system:

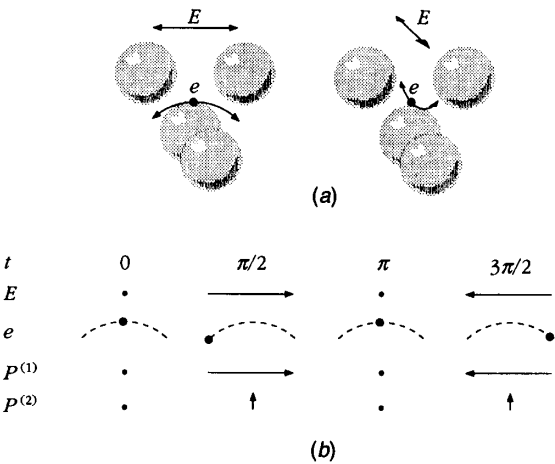


Figure 18 (a) An electron in the interstitial region between four atoms oscillates along a curved equipotential plane. (b) This oscillation causes a small second-order dipole in a direction perpendicular to the first-order dipole. The period of oscillation of the second-order dipole is one-half that of the first-order one.

$\omega_1 - \omega_2 = \omega_{res}$. The beating between the two input beams then coherently populates the upper level of the resonance. A third beam at frequency ω_3 then beats with the resonant oscillation in the system, generating a fourth beam at the anti-Stokes Raman frequency $\omega_a = \omega_1 - \omega_2 + \omega_3$. Note that this process is parametric, *i.e.*, the initial and final state is the same. The intensity of the coherent anti-Stokes beam is proportional to the population difference between the lower and upper levels of the resonance.[6] Hence, CARS can be used to measure population distributions.

Applications of nonlinear spectroscopy are summarized schematically in Figure 19.

III. ELECTRONIC AND VIBRATIONAL STATES OF SOLIDS

The atoms in a metal or semiconductor form an approximately regular three-dimensional pattern. Common arrangements of the atoms include face centered cubic (FCC) and body centered cubic (BCC), depicted in Figure 20, though many others are also common.[7] The energies of the states occupied by valence electrons depend on the arrangements of the atoms because valence electrons from neighboring atoms interact. The states of the valence electrons determine many properties of solids.

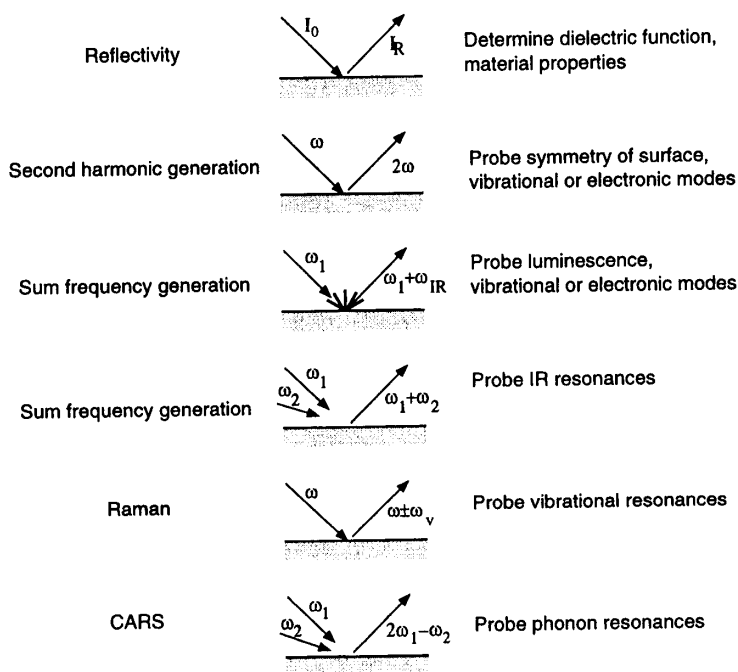


Figure 19 Schematic representation of some optical probes and their most important applications. Many phenomena can be studied with several different optical techniques. For example, vibrations can be studied with sum frequency generation, Raman scattering, and coherent anti-stokes Raman spectroscopy (CARS).

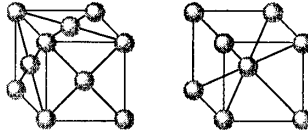


Figure 20 The face centered cubic (FCC, *left*) and body centered cubic (BCC, *right*) crystal structures. Not all the atoms are visible. The actual crystal is comprised of many of these cubes packed next to each other so that the atoms in the corners are shared by eight different cubes.

The wavefunction of an electron in a crystal is determined by the Schrödinger Equation 8 with $U(\vec{r})$ representing the potential of the charges in all the atoms. The equation cannot be solved analytically unless the real $U(\vec{r})$ is replaced with a simple function. Here we consider simple models to obtain a qualitative understanding of electronic states of solids.

III. A. Free electron states

We begin by considering free electrons for which $U(\vec{r}) = 0$. In the free electron model the Schrödinger equation yields a parabolic relationship between kinetic energy and momentum:

$$E = \frac{\langle p \rangle^2}{2m}. \quad (62)$$

This equation is called a dispersion relation; it relates the energy of the electron to its momentum. The momentum of the free electron can take on any positive value, and hence the energy of the electron can be anywhere from zero to infinity. Equation 62 is represented in Figure 21 for a one dimensional crystal.

When $U(\vec{r})$ is not zero, a theorem known as Bloch's theorem constrains the electronic wavefunction. The theorem applies to electronic states in a periodic potential $U(\vec{r})$ where

$$U(\vec{r} + \vec{R}) = U(\vec{r}) \quad (63)$$

for all \vec{r} . The vectors \vec{R} which satisfy (63) are called lattice vectors. Bloch's theorem states that when (63) is satisfied there exists a vector \vec{k} such that

$$\Psi(\vec{r} + \vec{R}) = e^{i\vec{k} \cdot \vec{R}} \Psi(\vec{r}). \quad (64)$$

This equation says that between points in the crystal separated by a lattice vector \vec{R} , only the (complex) phase of the wavefunction may change. Wavefunctions in a periodic potential satisfy (64) and are called Bloch wavefunctions.[7, 8]

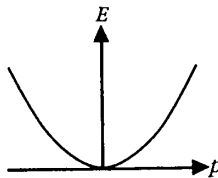


Figure 21 The parabolic dependence of energy on momentum for a free electron.

The quantity $\hbar\vec{k}$ is known as the crystal momentum. There are special values of the crystal momentum called reciprocal lattice vectors, \vec{K} , that satisfy

$$\vec{R} \cdot \vec{K} = 2\pi n, \quad (65)$$

where n is an integer. We may write a general \vec{k}' in terms of \vec{K} :

$$\vec{k}' = \vec{k} + \vec{K}. \quad (66)$$

When this expression is substituted into (64), the definition (65) ensures that the factor containing \vec{K} is 1:

$$\begin{aligned} \Psi(\vec{r} + \vec{R}) &= e^{i\vec{k}' \cdot \vec{R}} \Psi(\vec{r}) \\ &= e^{i(\vec{k} + \vec{K}) \cdot \vec{R}} \Psi(\vec{r}) \\ &= e^{i\vec{k} \cdot \vec{R}} \Psi(\vec{r}) \end{aligned} \quad (67)$$

Equation 67 is the same as Equation 64. Therefore, two crystal momenta, \vec{k}' and \vec{k} , which differ by a reciprocal lattice vector, \vec{K} , place the same constraints on the Bloch wavefunction. We therefore restrict attention to a small set of \vec{k} values called the *first Brillouin zone*, comprised of those \vec{k} whose magnitude cannot be made smaller by addition of a reciprocal lattice vector.

Bands are typically drawn only within the first Brillouin zone. Figure 22 shows an example in one dimension. The wave vectors \vec{k}' and \vec{k} differ by a reciprocal lattice vector of length $2\pi/a$. The horizontal arrows represent translations of the bands back into the first Brillouin zone. This representation is called the *reduced zone scheme*.

In a real crystal, the first Brillouin zone has a three-dimensional shape that reflects the symmetry of the real three-dimensional crystal lattice. Figure 23 depicts the first Brillouin zone of a FCC crystal. Conventional labels for points of high symmetry on the surface are indicated. There are many points on the surface that are equivalent to the labeled points because of the symmetry of the first Brillouin zone (and the crystal). The center of the polygon, $\vec{k} = 0$, is known as the Γ -point.

In a three-dimensional crystal, the \vec{k} are three-dimensional and a graph of the band structure can no longer represent the states at all \vec{k} . Instead, the bands are shown along particular directions in \vec{k} -space. Figure 24 shows the band structure for free electrons in a FCC lattice in the directions of highest symmetry. The horizontal axis uses labels defined in Figure 23. Some locations in k -space (such as the Γ -point) are represented more than once.

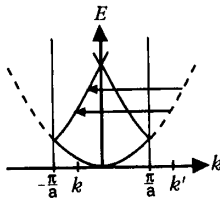


Figure 22 Wavevectors which differ by a reciprocal lattice vector (such as k and k') are physically equivalent. This motivates translating (represented by the horizontal arrows) the portions of the band that lie beyond $2\pi/a$ to produce a reduced zone representation.

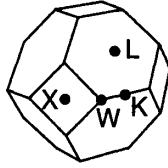


Figure 23 The first Brillouin zone of a FCC crystal. This is a figure drawn in three-dimensional k -space. The origin, $\vec{k} = 0$, is located at the center of the polygon and is called the Γ -point. Other points of high symmetry on the outer surface of the figure are labeled with letters as shown.

For example, the band structure is represented along three different paths from the Γ -point to the edge of the Brillouin zone: $\Gamma \leftrightarrow X$, $\Gamma \leftrightarrow L$, and $\Gamma \leftrightarrow K$.

At the Γ -point, for energies near $E = 0$, the bands in Figure 24 have the quadratic dependence of Equation 62. When the bands reach the first Brillouin zone boundary (at X, L, or K for example), they are translated back into the first Brillouin zone, producing an apparent reflection of the parabolic shapes about the X, L, and K points. This reflection is analogous to that sketched in Figure 22 for a one-dimensional crystal.

The shape of the parabola depends on the particular path chosen in k -space. According to the dispersion relation (62), the energy of free-electron states depends on the square of the magnitude of \vec{k} . This fact explains the kink in the graph at L between Γ and W: the distance from the Γ -point increases more quickly between Γ and L than between L and W, as apparent in Figure 23. Throughout Figure 24, the bands reflect the dispersion relation for free electrons and the geometry of the first Brillouin zone.

The bands are not necessarily occupied with electrons. They cannot all be filled because the number of electrons in the crystal is finite, whereas there are infinite states available in the band structure. The probability that a state of energy E is occupied is given by the Fermi-Dirac function,[7]

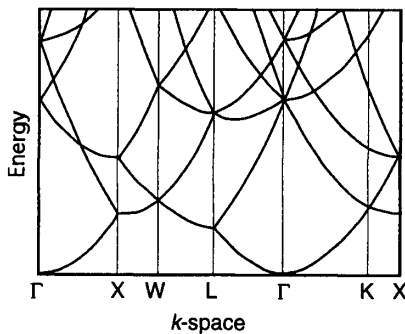


Figure 24 Free electron states for a FCC crystal. The states are plotted against representative directions in k -space. High symmetry positions in k -space are labeled with letters defined in Figure 23.

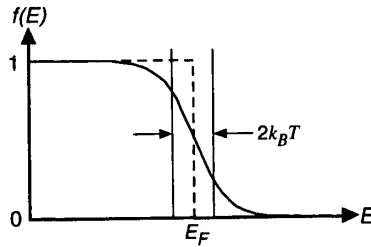


Figure 25 The Fermi-Dirac function at $T = 0$ (dashed line) and $T = 0.1E_F$ (solid line). The transition between $f(E) = 1$ and $f(E) = 0$ occurs over an energy range of approximately $2k_B T$.

$$f(E) = \frac{1}{e^{(E-E_F)/k_B T} + 1}, \quad (68)$$

where E_F is the Fermi energy, k_B is the Boltzmann constant, and T is the electron temperature. At $T = 0$, the Fermi-Dirac function is a step function: states below the Fermi energy are occupied and states above the Fermi energy are empty. At real temperatures the transition is smoother, as depicted in Figure 25. A Fermi-Dirac distribution is valid only when the electrons are in thermal equilibrium and temperature is well-defined.[8] Electrons out of thermal equilibrium are considered in the section on electron-electron scattering below.

In this section we have applied Bloch's theorem to determine how the symmetry of the crystal governs the electronic band structure. We have also assumed that the electrons are free, $U(\vec{r}) = 0$. These assumptions are, strictly speaking inconsistent. We see below, however, that when $U(\vec{r})$ is small but nonzero, the band structure resembles the free electron band structure. An excellent approximation of the band structure is obtained by applying only our knowledge of the symmetry of the crystal potential, (63) ignoring any interaction of electrons with the lattice.

III. B. Beyond free electron states

In a real crystal the electrons interact with the periodic potential of the lattice. The simplest band structures occur in metals where $U(\vec{r})$ is small. Recall that monovalent metals have a single electron outside a filled shell (or a filled sub-shell, such as Cu) and that this electron is shielded from the nucleus by its interactions with the other electrons. The shielding leads to relatively weak interactions with the lattice and small $U(\vec{r})$ compared to other crystals. We expect the band structure of monovalent metals such as K and Cu to be approximately the band structure of free electrons.

Figure 26 is a graph of the solution to the Schrödinger equation obtained from perturbation theory[1] with the weak periodic potential $U(\vec{r})$. The influence of the interactions with the lattice is to segment and distort the free-particle solution (Figure 22). The distortion occurs near the Brillouin zone boundary; in other regions the bands remain parabolic. Alkali metals have bands which are very similar to Figure 26.

In other metals, there are often bands with free-electron character. For example, the bands of aluminum (configuration [Ne] $3s^2 3p^1$) depicted in Figure 27 are very similar to free electron bands. Copper, with configuration [Ar] $3d^{10} 4s^1$, has a more complicated band

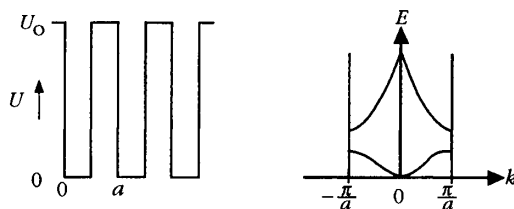


Figure 26 A periodic potential in one dimension (*left*) and the corresponding bands (*right*).

structure. The band structure of copper in Figure 28 has both horizontal and parabolic bands. The roughly horizontal bands arise from electrons in d -orbitals. The bands are horizontal because d -orbital electrons from one atom interact strongly with neighboring atoms, as expected from the graph of the spatial distribution of d -orbitals in Figures 3 and 5. The roughly parabolic bands in Figure 28 arise from the electrons in s -orbitals. The s -orbital electrons interact less with the lattice than the d -orbitals because of the small radial extent of s -orbitals. The parabolic bands in Figure 28 are similar to the free electron bands in Figure 24.

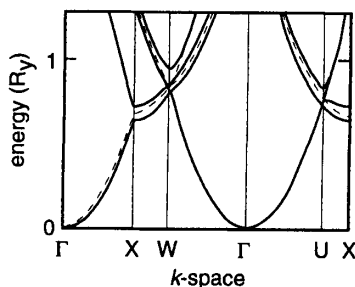


Figure 27 The band structure of aluminum has a lot of the parabolic character of free-electron bands. The dashed lines indicate the free electron bands. After [9]

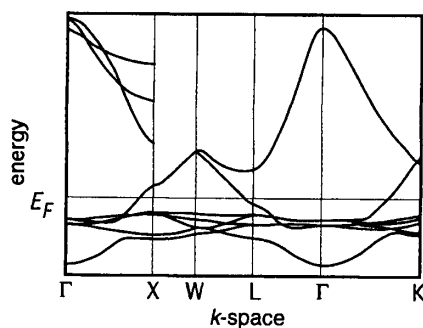


Figure 28 The calculated band structure of copper in a portion of k -space. Both parabolic free-electron-like bands and roughly horizontal d -bands are present. After [10].

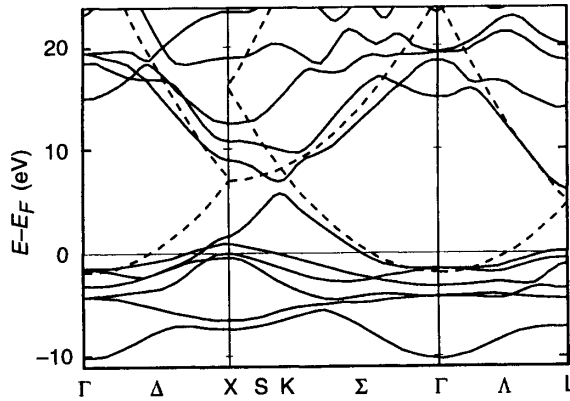


Figure 29 The calculated (solid lines) band structure of platinum. The dashed lines indicate the free electron bands for an FCC crystal. After [11]

The band structures of *d*-band metals share a number of features. Compare, for example, the band structure of copper in Figure 28 with the band structure of platinum shown in Figure 29. At low energy near the Γ -points, the quasi-free electron bands are similar because they are both FCC crystals. The Fermi levels of platinum and copper are at different locations with respect to the bands. In platinum (with configuration $[\text{Xe}] 4f^{14}5d^{10}6s^0$) the Fermi level is in the horizontal *d*-bands, while in copper the Fermi level lies in the parabolic *s*-bands.

III. C. The dielectric function of metals

In section II.B, we studied the relationship between the energy (or frequency) of an electromagnetic wave propagating in a material, and the dielectric function, $\epsilon(\omega)$ of the material. We derived the dielectric function for a material in which the electrons act as simple harmonic oscillators. Here we use that model to explain some features of the measured dielectric function of alkali metals, Figure 30. Additional features can be explained using the band structure of the alkali metals, Figure 31. More detailed structure of $\epsilon(\omega)$ can be predicted from the band structure than from the simple harmonic oscillator model because the band structure is a more complete description of the electronic states in the crystal lattice.

The interaction of light with the electrons in a material is represented by transition of electrons from occupied to unoccupied states in the band structure. According to the Fermi-Dirac function, Equation 68, unless the temperature is very high, occupied states are below the Fermi level, and unoccupied states are mostly above the Fermi level. If the initial and final states of the electron are in the same band, the transition is intraband. If the transition is from one band to another, the transition is interband. In both cases, the transition is from below the Fermi level to above the Fermi level.

In both intraband and interband transitions, the crystal momentum is conserved. When the crystal momentum of the electron changes, as it must in an intraband transition, one or more other bodies must have an opposite change in crystal momentum. The photon does not contribute to conservation of crystal momentum because photons have negligible momentum. Phonons, on the other hand, do have crystal momentum, and intraband transitions are usually

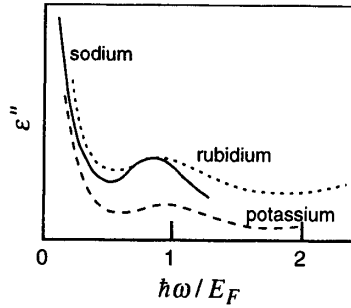


Figure 30 The experimentally determined imaginary parts of the dielectric function for the alkali metals. They are similar because the band structures are similar. After [8]

accompanied by excitation of a phonon. The total change in crystal momentum of the phonon and the electron is zero. Phonons are discussed in section III.E.

Intraband transitions are responsible for the decrease in $\epsilon''(\omega)$ with increasing frequency in Figure 30. According to Figure 31, low energy excitation of electrons near the Fermi level occur in an approximately parabolic band. From Figure 21, we know that electrons in parabolic bands behave as free electrons, and from Figure 17 from section II.B, we know that in a material with free electrons the imaginary part of the dielectric function drops with increasing frequency. The dielectric function of alkali metals is similar to the dielectric function of free electrons because the band structure is nearly parabolic near the Fermi level.

The dielectric functions in Figure 30 do not monotonically decrease. The increase in $\epsilon''(\omega)$ is attributed to the onset of interband transitions at energies sufficient to excite electrons across the gap between bands. The lowest energy interband transition (at constant crystal momentum) is shown in Figure 31. There are no transitions right at the Brillouin zone boundary because there are no electrons at the N-point: the Fermi level is below the energy at the N-point. The length of the arrow is about $0.65 E_F$. The onset of interband transitions accounts for the rise in $\epsilon''(\omega)$ in Figure 30 near $0.65 E_F$.

Figure 32 shows the measured real and the imaginary parts of the dielectric function of platinum.[12] Overall, $\epsilon''(\omega)$ falls with increasing energy—the expected free electron contribution to $\epsilon''(\omega)$. The structure at about 0.8 eV, is attributed to the onset of interband transitions near the X point in the platinum band structure, Figure 29.[13]

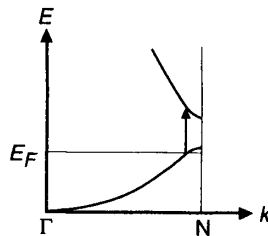


Figure 31 The band structure of an alkali metal, with an interband transition indicated. In an intraband transition (not shown) the initial and final states of the electron lie in the same band. After [8]

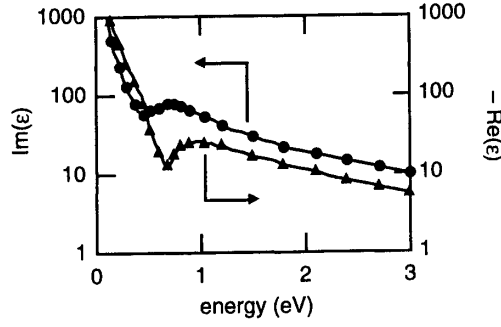


Figure 32 The dielectric function of platinum. The features at about 3/4 eV can be attributed to the band structure. Data from [12].

III. D. Electron-electron scattering

The electrons in a material do not necessarily have a distribution of energies described by the Fermi-Dirac equation. During absorption of light, for example, electrons acquire energies far in excess of $k_B T$. This energy is partitioned among all the electrons by collisions between electrons, until the distribution of electron energies is a Fermi-Dirac distribution. Fermi liquid theory predicts the rate at which a single electron excited above the Fermi level collides with another electron. One of the aims of the model is to predict the rate at which the excited electron scatters with other electrons.

Consider the collision of an excited electron of crystal momentum \vec{k}_1 with an electron of crystal momentum \vec{k}_2 , depicted in Figure 33. The scattering rate depends on the probability of finding an electron of momentum \vec{k}_2 , and also on the probability that there are empty states of momenta \vec{k}_1' and \vec{k}_2' . In Fermi liquid theory it is assumed that, except for the single excited electron in question, the distribution of electron energies is described by the Fermi-Dirac function, Equation 68. With this assumption we can write the scattering rate as:

$$\frac{1}{\tau} \propto f(\vec{k}_2) [1 - f(\vec{k}_1')] [1 - f(\vec{k}_2')]. \quad (69)$$

This is the scattering rate for a particular \vec{k}_1' and \vec{k}_2' . The scattering rate into all possible final states \vec{k}_1' and \vec{k}_2' depends on the total number of available states for \vec{k}_1' and \vec{k}_2' .

We estimate the number of available states when the temperature is zero Kelvin. The calculation begins with some observations about the relative energies of the electrons before and after the collision. Figure 25 implies that the final states \vec{k}_1' and \vec{k}_2' must satisfy

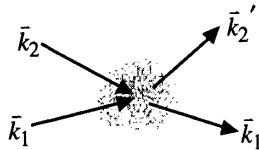


Figure 33 A binary collision between two electrons.

$E(\bar{k}_1') > E_F$ and $E(\bar{k}_2') > E_F$ because all the available (empty) states are above the Fermi level. The figure also implies that $E(\bar{k}_2) < E_F$ because the electron \bar{k}_2 must begin in an occupied state. Since the collision increases the energy of the electron \bar{k}_2 , the energy of the electron \bar{k}_1 must decrease to conserve energy: $E(\bar{k}_1') < E(\bar{k}_1)$. By a similar argument, the final energy of the electron \bar{k}_2 must be less than the initial energy of the excited electron: $E(\bar{k}_2') < E(\bar{k}_1)$. Both electrons end up with energies between E_F and $E(\bar{k}_1)$.

The number of available states between E_F and $E(\bar{k}_1)$ is proportional to $|\bar{k}_1| - |\bar{k}_F|$. Substituting this expression into (69) gives a scattering rate:

$$\frac{1}{\tau} \propto (|\bar{k}_1| - |\bar{k}_F|)^2. \quad (70)$$

This expression is valid when $T = 0$ and the initially excited electron \bar{k}_1 is near the Fermi level. Equation 70 shows that the lifetime of an electron becomes very large as the electron gets close to the Fermi level. Calculations of the scattering rate give electron-electron scattering times of 10 fs for an electron which lies 2 eV above the Fermi surface, and 1 ps for an electron which lies 0.2 eV above the Fermi surface. Equation 70 is often stated in terms of energy:

$$\frac{1}{\tau} \propto [E(\bar{k}_1) - E_F]^2. \quad (71)$$

Equations 70 and 71 are equivalent for energies close to the Fermi level.

At small (nonzero) temperatures the total number of states available for the electrons to scatter to depends on temperature. To calculate the scattering rate, we note that Figure 25 shows that the Fermi-Dirac distribution changes from 1 to 0 over a range of energies of order $k_B T$. If the target electron is to scatter into an available (empty) state, it must have an initial energy within the range $k_B T$ of E_F . Similarly, the number of available states scales as $k_B T$. Once the initial and final energies of the target electron are specified $E(\bar{k}_1')$ is known because of energy conservation. The scattering rate depends the square of the temperature:

$$\frac{1}{\tau} \propto (k_B T)^2. \quad (72)$$

In practice, the scattering of electrons with energy close to E_F is dominated by scattering with phonons (see below) or impurities, and the quadratic dependence of scattering rate on temperature is not observed.[8]

III. E. Phonons

In the previous two sections we assumed the ionic lattice to be fixed and immobile. In this section we consider collective motions of the ions. The ions can be displaced from their equilibrium positions and such disturbances can travel through the solid in the form of phonons which play an important role in the electronic and optical properties of solids because they can interact directly with electromagnetic waves.

Let us begin by considering a linear chain of identical atoms separated by a spacing a as illustrated in Figure 34. The top of the drawing shows the atoms in their equilibrium position; at the bottom the atoms are displaced from their equilibrium position. Let us assume that only nearest neighbors exert forces on each other and that the interionic force obeys Hooke's law. The forces exerted on ion n by its two nearest neighbors are thus

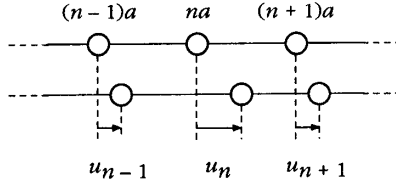


Figure 34 Vibrating linear chain of identical atoms spaced by a distance a .

$$\begin{aligned} F_{n-1,n} &= \gamma(u_{n-1} - u_n) \\ F_{n+1,n} &= \gamma(u_{n+1} - u_n) \end{aligned} \quad (73)$$

where γ is the force constant. The equation of motion for the ion is then

$$m \frac{d^2 u_n}{dt^2} = \gamma[u_{n-1} + u_{n+1} - 2u_n]. \quad (74)$$

We look for solutions in the form of a traveling harmonic displacement wave (called a normal mode)

$$u_n(t) = A e^{i(qna - \omega t)}, \quad (75)$$

where A is the amplitude of the displacement wave, q the wavevector, and ω the angular frequency. Substituting this into Equation 74 we get

$$-m\omega^2 = \gamma[e^{-iqa} + e^{iqa} - 2] = -4\gamma \sin^2\left(\frac{qa}{2}\right), \quad (76)$$

so

$$\omega = \sqrt{\frac{4\gamma}{m}} \left| \sin \frac{qa}{2} \right|. \quad (77)$$

As Figure 35 shows, we only need to consider displacement waves of wavelength larger than $2a$ — due to the discreteness of the chain, all waves of shorter wavelengths are equivalent to certain waves of longer wavelengths. This means we can restrict our analysis to small wavevectors:

$$\lambda \geq 2a \Rightarrow q \leq \frac{\pi}{a}. \quad (78)$$

Figure 36 shows the dependence of the displacement frequency on wavevector q (77). For small wavevector, Equation 77 becomes linear in the wavevector

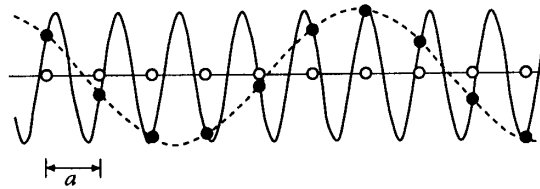


Figure 35 Oscillating chain of atoms showing instantaneous displacements. The solid curve conveys no information not given by the dashed one.

$$\omega = \sqrt{\frac{4\gamma}{m} \frac{qa}{2}} = \sqrt{\frac{\gamma a}{m/a}} q = v_s q, \quad (79)$$

with v_s the speed of sound. This is the relation one would obtain if the chain were continuous rather than discrete (when a approaches zero, π/a goes to infinity and the dispersion relation becomes linear throughout). The dispersion of waves near the edge of the Brillouin zone at π/a is therefore a direct consequence of the granularity of the chain.

In a two-atom linear chain the situation is more complicated because the atoms of different kind can either move in phase (such displacement waves are called acoustic phonons) or out of phase (optic phonons). Figure 37*a* illustrates the displacements that occur for transverse acoustic (TA) and optic (TO) phonons of small wavevector. While both displacements have the same large wavelength, the potential energy associated with the optic phonon is larger because the interatomic bonds are much more distorted. The dispersion relation now has two branches (see Figure 38*a*); for low wavevector the acoustic branch approaches zero, but because of the large distortion at low frequency, the corresponding energy for the optic branch is nonzero at zero wavevector.

Figure 37*b* shows the displacements for the acoustic and optic phonons of the shortest possible wavelength ($\lambda = 2a$). The corresponding energies (see Figure 38*a*) are slightly different. Figures 37*c* and 37*d* show how the cases illustrated in Figs. 37*a* and 37*b* relate to single-atom chain phonons: the optic branch vanishes as low wavevector optic phonons map onto large wavevector acoustic phonons. Note, in particular that the low- q TO phonon for the two-atom chain maps to a high- q TA phonon on the one-atom chain (*cf.* Figs. 37*a* and *c*). Similarly, the TO and TA phonon modes at the edge of the Brillouin zone for the two-atom chain, are identical on the one-atom chain (*cf.* Figs. 37*b* and *d*), but are now in the middle of a Brillouin zone that is twice as wide (Figure 38*b*).

III. F. Electron-phonon interaction

The Bloch wavefunctions (64) are solutions to the Schrödinger equation only when the

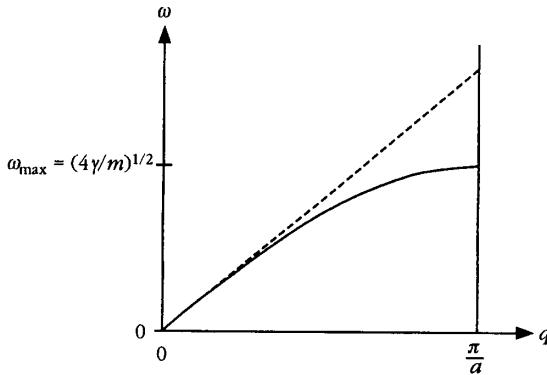


Figure 36 Dispersion of waves along a linear chain of atoms. The dashed line shows the result one would obtain for a continuous medium. The slope of the dashed line corresponds to the speed of sound waves in the medium.

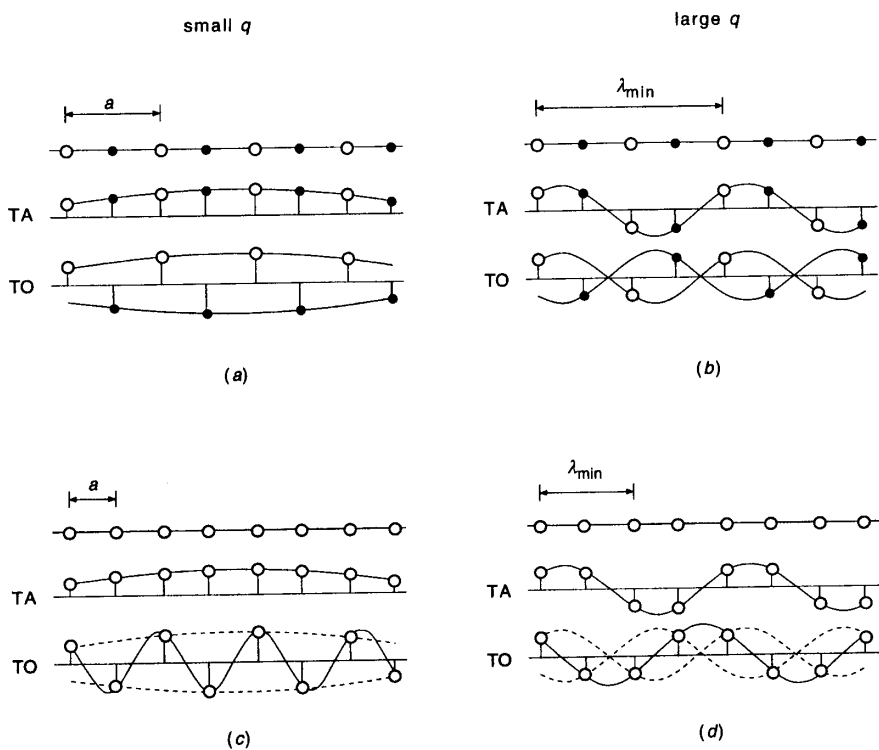


Figure 37 Waves on two-atom linear chains. Displacements are shown for (a) small and (b) large wavevector. The in- and out-of-phase waves correspond to acoustic and optic phonons, respectively. The bottom to graphs (c) and (d) show how the waves for a two-atom chain map onto waves of different wavevector for a one-atom chain.

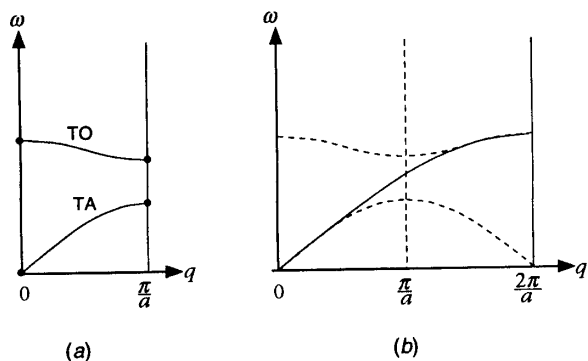


Figure 38 Dispersion relation for phonons (a) on a two-atom linear chain and (b) on a corresponding one-atom linear chain.

lattice is perfectly well ordered. In practice phonons cause a distortion of the lattice. The distortion allows electrons to make transitions between Bloch states. This process is described as a scattering of an electron with a phonon, and can either transfer energy to the phonon or to the electron.

We consider a phenomenological treatment of this scattering relevant when the electrons have been very highly excited by a laser pulse. For example, when a subpicosecond laser pulse with photon energy of about 2 eV strikes a metal surface, the energy is absorbed by the electrons. The electrons share this energy among themselves by electron-electron collisions (see above), reaching a Fermi-Dirac distribution. Simultaneously, the electrons scatter with phonons, effectively heating the metal. The spatial variation in the deposited laser energy creates a complication: the energy diffuses away from the surface towards the bulk.

These ideas are expressed in a model for the response of a metal to ultra-fast photo-excitation.[14, 15] This model states that the temperatures of the electrons, T_e , and phonons (the lattice), T_l , evolve according to:

$$\begin{aligned} C_e(T_e) \frac{\partial T_e}{\partial t} &= \kappa(T_e) \frac{\partial^2 T_e}{\partial x^2} - g(T_e - T_l) + A(x, t) \\ C_l(T_l) \frac{\partial T_l}{\partial t} &= g(T_e - T_l) \end{aligned} \quad (80)$$

where $A(x, t)$ is the energy deposited by the laser and C_e and C_l are the heat capacities of the electrons and the lattice. The constant g determines how quickly the electrons and phonons thermalize with each other. The first equation contains a term describing the diffusion of the electrons. The energy carried by phonon diffusion is small compared with that due to electron diffusion in a metal; phonon diffusion is neglected in this model. The constants are approximately known, and so the electron and lattice temperatures can be found by numerical solution of Equation 80.

Figure 39 shows the evolution of the electron and lattice temperatures at the surface of platinum following excitation by a $32 \mu\text{J}/\text{mm}^2$, 800-nm pulse. Initially the sample is in thermal equilibrium at 90 K. The laser pulse causes a large transient rise in the surface electron temperature followed by equilibration of the electron and lattice temperatures in a few picoseconds.

This model assumes that the electrons are always thermalized with each other—that they satisfy a Fermi-Dirac distribution at all times. In reality the laser pulse excites electrons far above the Fermi level and a finite time is required for the electrons to thermalize. For example, 800 nm photons have 1.6 eV energy, while at 90 K, $k_B T \approx 8 \text{ meV}$. The relaxation of the photo-excited electrons to a Fermi-Dirac distribution has been the subject of numerous experiments.[16-19]

III. G. Photoemission spectroscopy

One of the most direct experimental methods for determining electronic states is photoemission spectroscopy, illustrated in Figure 40. Light stimulates an electron in a solid. If the electron is sufficiently excited, it escapes the material with energy

$$E_k = \hbar\omega - \Phi - E_i. \quad (81)$$

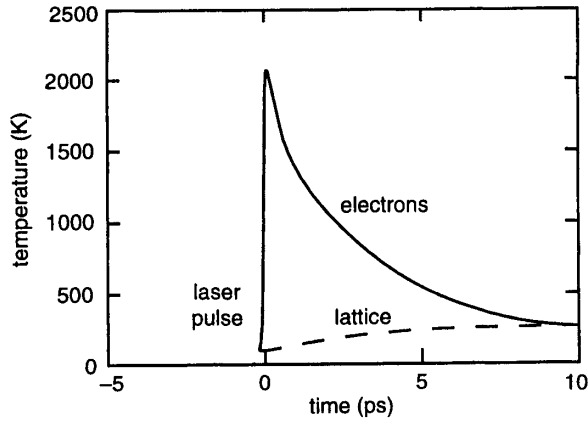


Figure 39 Calculated evolution of electron and lattice temperatures following excitation of platinum with a 100-fs, $32 \mu\text{J}/\text{mm}^2$, 800-nm laser pulse.

The energy of the photo-emitted electron depends on the initial photon energy, $\hbar\omega$, the initial state energy, E_i , and the energy required to extract the electron from the material, Φ , known as the work function. By measuring E_k , the energy of the initial state can be inferred. Generally electrons are emitted over a range of electron energies corresponding to the range of occupied states in the band structure, and the electrons comprise a photoelectron spectrum, as sketched in Figure 40.

The states that are probed in a photoemission experiment depend on the source of the initial excitation. Figure 41 depicts the some of the features which are observed with different excitation sources.

When the photon energy is low, the electrons may not receive enough energy from a single photon to overcome the work function of the material., but may escape if stimulated by two photons. This two-photon photoemission, or TPPE, is used to study the electronic states which lie between the Fermi level and the vacuum level. Because these states are above the Fermi level, the electrons rapidly scatter out of these states; TPPE using short pulses can therefore be used to study the dynamics of electron relaxation. Another way to study states between the Fermi level and the vacuum is to apply a strong DC electric field to the sample

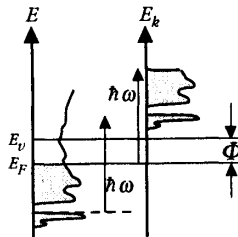


Figure 40 In photoemission spectroscopy the kinetic energy, E_k , of the emitted electron (right side of figure) depends on the initial state of the electron (left side of figure), the photon energy, and the work function. After [20].

surface. The potential barrier between an electron at the surface and a free electron in vacuum can be overcome if the applied field is sufficiently large.

At the other extreme, x-ray photons with energies in the 1000–eV range can eject core-level electrons. The resulting vacancy in the core level may be filled by an electron from a valence level. The energy released by this transition from the valence level to the core level may be imparted to another valence electron which is then ejected from the material with an energy depending on the energy levels of the states involved. This process is known as Auger recombination. The photoelectron spectrum following x-ray excitation has peaks which directly reflect the energies of the core levels, and peaks which arise from Auger recombination and reflect the energies of the valence and core levels. Spectroscopic techniques that rely on core-level ionization often use a monochromatic beam of electrons as the excitation source because electron-beam sources are conveniently produced in the laboratory from hot filaments.

The escape of an electron from the surface is not always as simple as depicted in Figure 40. The electrons may scatter and lose some of their energy. These collisions lead to a broad distribution of electron energies. When these electrons escape the surface, they are known as secondary emission. Secondary emission is observed as a broad feature at low E_k . The scattering of electrons accounts for the surface sensitivity of photoemission spectroscopy: only electrons emitted in the near surface region escape the material and are detected. The depth of the material that is probed with photoemission spectroscopy depends usually on the escape depth of the photoelectrons and not on the absorption length of the excitation source.

IV. A SURFACE SCIENCE PRIMER

This section is an introduction to the physics which governs chemical reactions at surfaces. Most of the examples are drawn from the chemistry of oxygen on platinum in preparation for section V of this chapter.

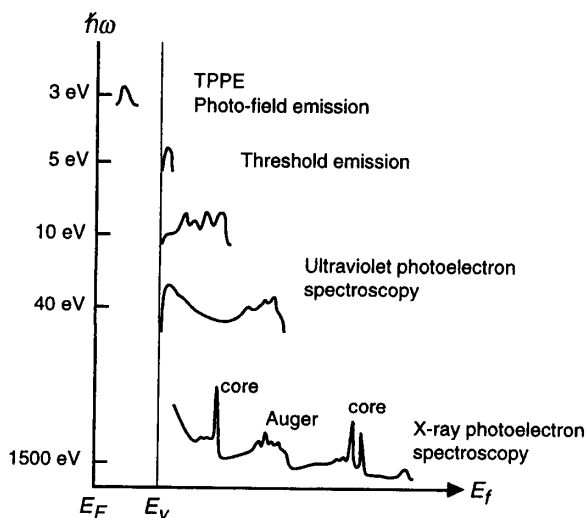


Figure 41 The photoelectron spectrum depends on the energy of the exciting photon. X-rays are able to induce emission of core electrons and Auger electrons. After [20]

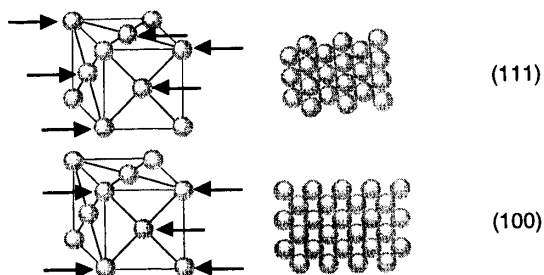


Figure 42 The (111) and (100) surfaces of an FCC crystal. The arrows indicate atoms in the crystal lattice which comprise the surface. In the diagrams of the crystals the spheres representing the atoms are not drawn to scale compared to the size of the cube.

Surface reactions are influenced by the chemical composition of the surface and the structure of the surface. To reduce the complexity, surface reactions are often studied on very clean, single crystal surfaces. A single crystal surface is cleaned in ultra-high vacuum (1×10^{-10} torr). Using the ideal gas law, one can calculate that at a pressure of 10^{-6} torr, approximately 1 s is required for every surface atom to be struck by a gas phase molecule.[21] Each such collision is an opportunity for a gas phase molecule to stick on the surface. Thus to maintain a surface clean for, say, 10^4 s a pressure near 10^{-10} torr is required.

The direction of the surface plane with respect to the lattice of a single crystal is specified by Miller indices.[7] Figure 42 shows examples of surfaces obtained from an FCC lattice. The (111) surface has a high density compared with the (100) surface. We concentrate our attention on the (111) surface of platinum, Pt(111).

IV. A. Sample preparation

Common procedures for cleaning a surface include annealing, and sputtering. The precise cleaning procedure is often determined by trial-and-error, using the diagnostic procedures described below to monitor the surface quality. As a starting point, there are compiled lists of the techniques that have been used to clean many crystals.[22]

When the sample is annealed in UHV (*i.e.* kept at elevated temperature for a certain time), some impurities simply desorb from the surface. For example, carbon monoxide desorbs from Pt(111) when the temperature exceeds about 300 K. Annealing may also provide the thermal energy required for surface atoms to rearrange themselves and correct small defects in the surface structure.

Sputtering is used to remove the first few layers of atoms from the surface. A noble gas, usually either neon or argon is admitted to the chamber. The gas is ionized and the ions are electrostatically accelerated to the surface. The ions dislodge material from the sample surface, including both the desired atoms and the impurities. This usually improves surface quality because impurities often cluster at the surface, particularly following annealing in vacuum or oxygen. Sputtering creates defects in the surface structure, so it is usually followed by annealing.

Pt(111) is usually cleaned by annealing in an oxygen atmosphere. During annealing, impurities such as silicon diffuse to the surface where they may bind with an oxygen atom, becoming trapped at the surface as an oxide. When these oxides are removed by sputtering,

the density of impurities in the near-surface region is reduced. Annealing in oxygen also reduces carbon contamination because the carbon reacts to form carbon monoxide which desorbs from the surface.

IV. B. Adsorption of reactants

There are two classes of interaction between a molecule and a surface. Chemisorption refers to a molecule or atom attached on a surface by a chemical bond. Physisorption is a much weaker van der Waals interaction between a molecule or atom and a surface. The energy which binds a chemisorbed species to a surface is typically 0.4–10 eV while physisorption energies are typically 0.01–0.1 eV.

To understand physisorption, picture a metal surface interacting with a polarized molecule or atom as shown in Figure 43. Whenever a charged species is placed near a metal surface its electric field causes an image charge in the metal.[23] The image charge is positioned so that the electric field produced by a charge and its image charge is identical to the field which would be produced by the charge and the true distribution of surface charge on the metal. Figure 43 depicts a polarized adsorbate as two charges separated by a distance u . The corresponding image charges are shown.

The interaction of the adsorbate with the surface may be determined by finding the total electrostatic (Coulomb) interaction between the charges in the adsorbate and the image charges in the metal:

$$\begin{aligned}
 U(z) &= -\frac{e^2}{4\pi\epsilon_0} \left[\frac{1}{2z} + \frac{1}{2(z-u)} - \frac{1}{(2z-u)} - \frac{1}{(2z+u)} \right] \\
 &\approx -\frac{e^2}{4\pi\epsilon_0} \frac{u^2}{z^3}.
 \end{aligned}
 \tag{82}$$

On the right side of this equation, the interaction potential $U(z)$ is expanded into a Taylor series for small u/z . The interaction potential, Equation 82, is zero if there is no polarization, $u = 0$. Otherwise the interaction varies as $1/z^3$.

When the adsorbate is very close to the metal, the image charge model shown in Figure 43 is not accurate because the interaction becomes repulsive. When the repulsive interaction is balanced against the attractive interaction of Equation 82, the adsorbate typically settles 0.3 – 1.0 nm from the surface in a shallow well. Physisorption is observed only at low temperatures. For example, O_2 will physisorb on Pt(111) at 45 K and form multiple physisorbed layers at 30 K.[24]

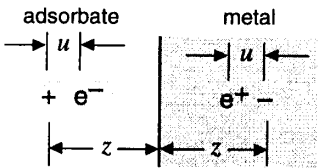


Figure 43 A polarized molecule or atom near a metal surface interacts with its image charges. After [21].

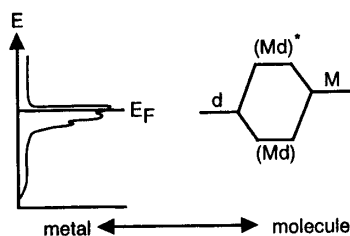


Figure 44 Chemisorption of a molecule on a metal surface is accomplished by mixing a d -orbital of the metal with an orbital of the molecule. Bonding (Md), and anti-bonding (Md)* orbitals are formed. After [21].

An adsorbate is chemisorbed if it forms a chemical bond with the substrate. The bond substantially changes the electronic states of the adsorbate. Figure 44 represents the energy levels of a molecule chemisorbed on a transition metal surface. The left side of the diagram represents the d -band of the transition metal. The right side represents a state of the free molecule. When the molecule chemisorbs on the metal surface the orbital of the molecule can mix with a d -orbital of the metal. The mixing is analogous to the formation of a bond between two atoms to make a molecule, Figure 9. The chemisorption of O_2 on Pt(111) is described in detail in section IV. F.

IV. C. Surface diagnostics

In the discussion of photoemission spectroscopy, we mentioned that electrons may be emitted from an atom by Auger recombination following removal of a core-level electron. The energy of the Auger electron depends on the energies of electronic states of the atom; since these energies are unique to each atom, the Auger spectrum identifies the atoms present in the sample. Auger spectroscopy is one of the most common means of determining chemical composition of a surface. Figure 45 shows the Auger spectrum obtained from a platinum surface. Interpretation of an Auger spectrum requires comparison of the observed spectrum with reference spectra from samples of known composition.[25]

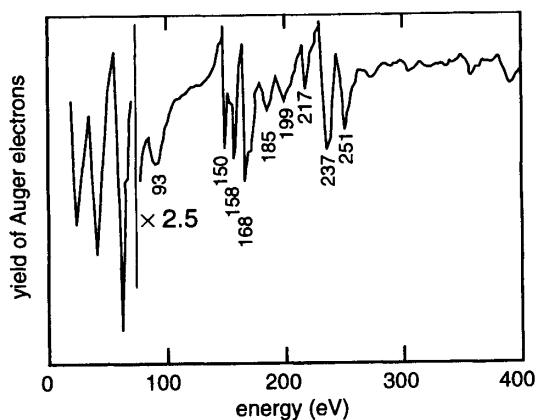


Figure 45 Auger spectrum of platinum. After [25].

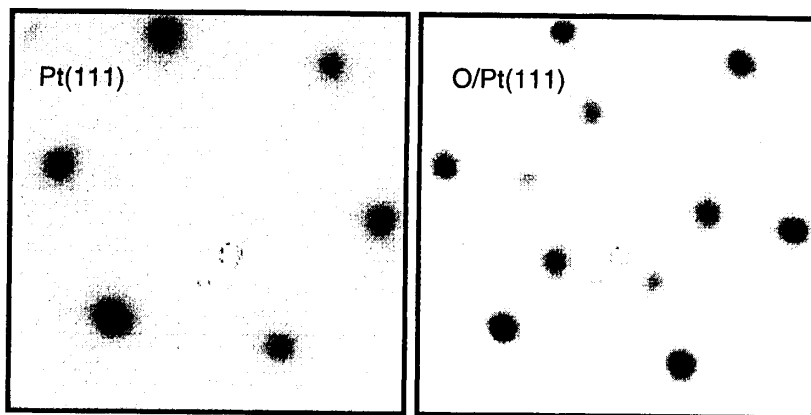


Figure 46 LEED patterns obtained from Pt(111), *left*, and O/Pt(111), *right*. The electron gun (not visible) obscures one of the spots due to oxygen.

Low energy electron diffraction (LEED) is used to determine the order of a surface. A monochromatic beam of electrons diffracts off the surface and is intercepted by a phosphor screen. The left side of Figure 46 shows the pattern formed by scattering of electrons from Pt(111). The hexagonal symmetry of the Pt(111) surface is reflected in the symmetry of the diffraction pattern. The right side of Figure 46 shows the diffraction pattern from a Pt(111) surface that has been exposed at 300 K to a few Langmuir of O₂: in addition to the diffraction spots due to the platinum atoms, there are spots attributed to diffraction of electrons from oxygen atoms. By comparing the positions of the spots due to oxygen to those due to platinum, it follows that the density of oxygen atoms is 1/4 the density of the platinum atoms. The oxygen atoms are arranged in a regular grid on top of the platinum surface; if their distributions were random they would not produce a sharp diffraction pattern.

The vibrational modes of an adsorbate can be probed by scattering a beam of monochromatic electrons off the sample. Some of the electrons lose energy by exciting discrete electronic or vibrational transitions in the adsorbates, so the distribution of adsorbate modes is reflected in the distribution of energies of the scattered electrons. The technique is called electron energy loss spectroscopy (EELS). Figure 47 shows the EEL spectrum of chemisorbed O₂ on Pt(111).[26-28] The signal at zero loss is 50 cm⁻¹ wide; this is the resolution limit. The signals at 875 cm⁻¹ and 700 cm⁻¹ are attributed to stretching of the oxygen molecule along the O–O bond axis.[26] The signal at 380 cm⁻¹ is assigned to vibration of the O₂ molecule perpendicular to the surface.[27] The signals at losses above 875 cm⁻¹ are attributed to electrons that excited multiple quanta of the surface modes or coupled modes. The vibration of atomic oxygen with respect to the Pt(111) would scatter electrons with a loss of 480 cm⁻¹. [26, 27]

Infrared (IR) spectroscopy is another way to study the vibrational modes of adsorbates. Infrared light reflected off the surface is absorbed at frequencies that are resonant with vibrational frequencies of the adsorbates. IR spectroscopy using short laser pulses has been employed to study the decay of vibration of adsorbates due to loss of vibrational energy to the substrate. The decay is complete in roughly one picosecond for adsorbates on metal surfaces.[29, 30] Very short laser pulses are used to resolve these timescales. Their intensities are high enough for the nonlinear optical spectroscopies that were summarized in Figure 19.

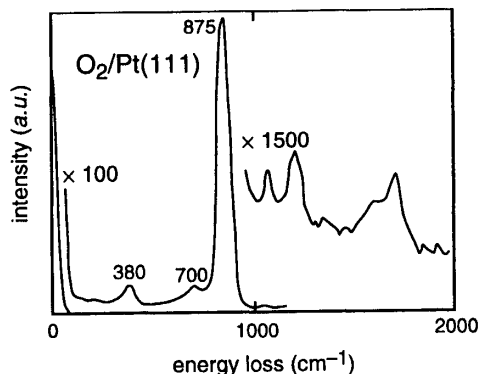


Figure 47 Electron energy loss spectroscopy of a saturated overlayer of O_2 on Pt(111) from a beam of 2 eV electrons incident at 75° . After [26]

The spatial distribution of surface electronic states can be imaged with atomic resolution by scanning tunneling microscopy (STM). The STM micrograph can be interpreted as a map of the surface because the electronic surface states are determined by the substrate and the adsorbates. In a recent study of the thermal dissociation of O_2 on Pt(111), an STM was used to determine that when O_2 thermally dissociates, the oxygen atoms break free of their mutual bond with enough kinetic energy to move approximately two platinum lattice constants.[31] This is experimental evidence that atoms can have ballistic motion on a surface. Below we summarize how the STM was used to determine the sites where O_2 chemisorbs on Pt(111).

IV. D. Thermal chemistry

We have seen that oxygen binds to platinum in several different forms: physisorbed molecular oxygen, chemisorbed molecular oxygen, and chemisorbed atomic oxygen. Because each form of oxygen is bound at a different site on the platinum with a different binding energy, these atoms become chemically active at different temperatures. A common way of studying adsorbate/substrate systems is to increase the sample temperature at a regular rate while monitoring the species desorbed from the surface. The experiment is called temperature programmed desorption (TPD) or temperature programmed reaction spectroscopy (TPRS) depending on whether the adsorbates simply desorb from the surface, or react to form new species. The yield in TPD or TPRS is plotted against the corresponding temperature, indicating the temperatures of thermally induced desorption and reaction.

Figure 48 shows the TPD of chemisorbed molecular oxygen, O_2 /Pt(111), obtained with a 4 K/s heating rate. The signal at 36 atomic mass units (amu), is due to oxygen molecules comprised of the 18 amu isotope of oxygen, $^{18}O_2$. The 140 K signal, called α - O_2 , is attributed to direct desorption of intact molecules. The O_2 desorption at 750 K, β - O_2 , shows that not all the oxygen desorbs at 140 K. If the TPD is stopped between the α - O_2 and the β - O_2 desorption signals, an EEL spectrum has features attributed to atomic oxygen, but none attributed to molecular oxygen. The LEED pattern is the pattern produced by atomic oxygen on Pt(111) (Figure 46, right side). These observations indicate that there is no molecular oxygen on the surface, but there is atomic oxygen. The β - O_2 signal must be due to recombination of oxygen atoms, known as recombinative desorption.

So far we have discussed adsorption of a single species. The final section of this paper discusses photo-induced reaction between two adsorbed species, CO and O₂ on Pt(111). Production of CO₂ can be induced with light or heat. Figure 49 shows the signal at 48 amu detected during TPRS of CO/O₂/Pt(111). The surface was prepared with the isotopes C¹⁸O and ¹⁸O₂, and so the signal at 48 amu is due to CO₂. The different peaks correspond to the CO interacting with oxygen atoms in different states. The first desorption peak, α -CO₂ is not observed during TPRS of CO coadsorbed with atomic oxygen, CO/O/Pt(111).[32] The α -CO₂ is attributed to reaction of CO with an oxygen atom created by O₂ dissociation, before this atom equilibrates with the surface.[33] The other CO₂ peaks, β -CO₂, are due to reaction between CO and atomic oxygen after the atomic oxygen has equilibrated with the surface. The reaction occurs as the CO and O diffuse on the surface, forming islands; the multiple peaks arise from reaction as the CO and O collide during different stages of this diffusion.[34]

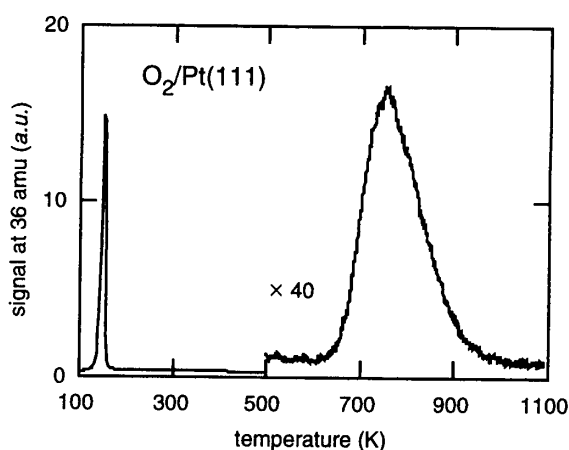


Figure 48 Temperature programmed desorption of O₂/Pt(111). The sample was dosed with isotopic oxygen, ¹⁸O₂, and the signal is detected at 36 amu with a mass spectrometer.

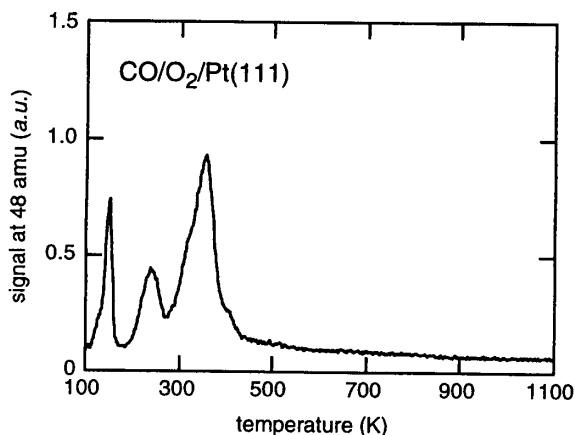


Figure 49 Temperature programmed reaction spectroscopy of CO/O₂/Pt(111). The signal at 48 amu is due to carbon dioxide, C¹⁸O₂.

IV. E. Isotope exchange

Isotopic labeling of reactants is used to determine pathways in surface reactions. Different isotopes of a molecule have different vibrational frequencies and therefore have different EELS spectra. With a mass spectrometer of resolution better than 1 amu, different isotopes of the same product are distinguishable in TPD and TPRS.

Figure 50 shows the application of isotopic labeling to the study of thermal reaction in $\text{O}_2/\text{Pt}(111)$. A mixture of 50% $^{16}\text{O}_2$ and 50% $^{18}\text{O}_2$ was prepared by mixing $^{16}\text{O}_2$ and $^{18}\text{O}_2$ outside the vacuum chamber. This gas was admitted to the sample surface to produce a chemisorbed overlayer denoted $(^{18}\text{O}_2, ^{16}\text{O}_2)/\text{Pt}(111)$. The left of Figure 50 shows the signal at 36 amu due to $^{18}\text{O}_2$ product. The α - O_2 signal is about half as large as in Figure 48, and the β - O_2 signal is about one quarter as large as in Figure 48. The signal at 32 amu due to desorption of $^{16}\text{O}_2$ looks very similar to the signal for $^{18}\text{O}_2$. The right side of Figure 50 shows the signal at 34 amu due to $^{16}\text{O}^{18}\text{O}$. There is no yield of α - $^{16}\text{O}^{18}\text{O}$, but comparison of the left and right sides of Figure 50 shows that the yield of β - $^{16}\text{O}^{18}\text{O}$ is twice as large as the yield of β - $^{18}\text{O}_2$. These observations are consistent with the evidence derived from EELS and LEED above. At 140 K, oxygen molecules desorb from the surface without opportunity to exchange isotopes of oxygen between molecules. Oxygen molecules also dissociate at 140 K. Near 700 K, the atoms recombine, but now there is opportunity for two different isotopes to form a molecule, $^{16}\text{O}^{18}\text{O}$. The probability of getting $^{18}\text{O}_2$ or $^{16}\text{O}_2$ at this stage is one half the probability of getting $^{16}\text{O}^{18}\text{O}$.

IV. F. Details of the bonding of oxygen to platinum

In the gas phase, molecular oxygen has 12 valence electrons in the $2\sigma_g$, $2\sigma_u^*$, $1\pi_u$, $3\sigma_g$, and $1\pi_g^*$ orbitals.[35] The right hand side of Figure 43 shows the electronic states of gas-phase O_2 which are most relevant to its bonding on platinum, including two π orbitals oriented normal to the molecular axis which have identical energies.

Experiments with scanning tunneling microscopes (STM) show that O_2 chemisorbs in at least three different configurations on $\text{Pt}(111)$. [36] The O_2 is observed over a bridge site between two platinum atoms with the O–O bond axis parallel to the surface and aligned to

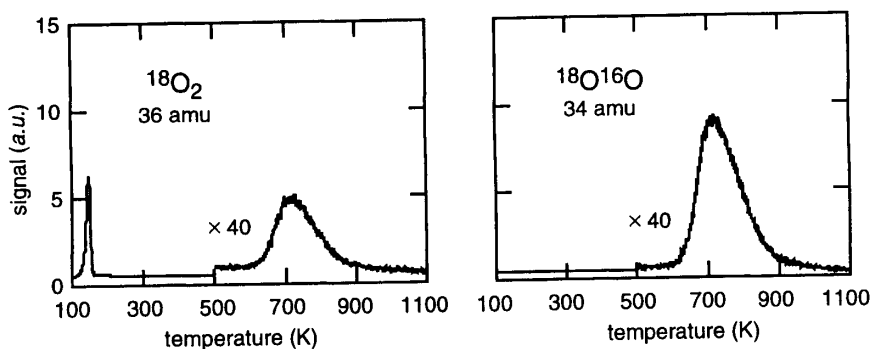


Figure 50 The TPD signal of (left) $^{18}\text{O}_2$ and (right) $^{16}\text{O}^{18}\text{O}$ from $(^{18}\text{O}_2, ^{16}\text{O}_2)/\text{Pt}(111)$. The yield of $^{16}\text{O}_2$ is very similar to the yield of $^{18}\text{O}_2$.

face the tops of platinum atoms. Calculations show that the O–O bond length in this configuration is 0.139 nm and the energy of vibration of the O–O bond is 850 cm^{-1} . [37] An O_2 species bound over FCC three-fold hollows is also observed with the STM. [36] Calculations show that this O_2 molecule is tilted 8° out of the plane of the surface. The O–O bond length is 0.143 nm and the energy of vibration is 690 cm^{-1} . [37] The calculated energies of vibration of the O–O bonds in the bridge and fcc configurations are consistent with observed vibrational energies from electron energy loss spectroscopy. The stretching of the O–O bond with respect to the 0.1207 nm length in the gas phase is consistent with the bond length inferred from x-ray spectroscopy. [38, 39] The stretching is due to transfer of electrons from the platinum into orbitals that are anti-bonding with respect to the O–O bond. The third O_2 species observed with STM is at O_2 adsorbed at step edges. [36, 40] Temperature programmed desorption experiments show that the binding energy of all the O_2 species is close to 0.4 eV. [27]

When the O_2 chemisorbs, some of the oxygen orbitals mix with platinum orbitals. The $1\pi^*$ orbitals perpendicular to the surface mix with the platinum d -band orbitals, producing π_b^* and π_g orbitals. The $1\pi^*$ orbitals of the oxygen parallel to the surface are not greatly perturbed and are denoted π_n . [39, 41] A shaded bar in Figure 51 represents the extent of the entire π_b and π_n region compiled from experimental [38, 42] and computational [41, 43, 44] sources. Overall, there is a net transfer of charge from the platinum to the O_2 . [27]

A surface layer of atomic oxygen on Pt(111) can be obtained by exposing the surface to molecular oxygen at platinum temperatures above 145 K. [46] The surface coverage saturates at 0.25 ML with a $p(2\times 2)$ LEED pattern. [27] The oxygen binds in fcc three-fold hollow sites, [47] with a 1.1 eV binding energy at 0.25 ML coverage, [27] and a 470-cm^{-1} Pt–O

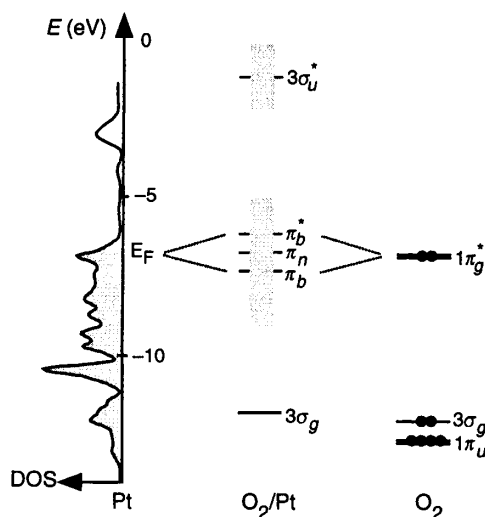


Figure 51 The calculated density of states of platinum [45] shown with the experimentally and theoretically determined states of O_2 chemisorbed on Pt(111). The vertical shaded bars indicate the approximate widths and locations of the orbitals of O_2 on the surface. Many of the O_2 orbitals are out of the energy range shown. [13]

vibration. Higher coverages of atomic oxygen can be attained by photodissociation of $\text{N}_2\text{O}/\text{Pt}(111)$, [48] or by electron-beam dissociation of $\text{O}_2/\text{Pt}(111)$. [26]

V. PHOTOCHEMISTRY OF OXYGEN ON PLATINUM

It has been well-established that high-intensity subpicosecond laser pulses induce reactions among adsorbates on a metal surface by photo-excitation of electrons in the metal substrate. [49-53] There is an active debate, however, about the energy distribution of the electrons responsible for the reaction between adsorbates on a metal surface. According to one proposal, the adsorbates interact with an essentially thermal substrate electron distribution. [54] According to another proposal the photon-energy-dependent electron distribution plays a significant role in the surface reactions. [52]

The yields in subpicosecond photo-induced reactions have a nonlinear dependence on fluence, a high quantum efficiency, highly-excited nonthermal internal-state distributions, and increasing translational energy with increasing laser fluence. [49, 51, 52, 54-59] Two-pulse correlation experiments show that the excitation has a lifetime of about 1 ps. [52, 58-61] Time-resolved surface second-harmonic generation indicates that desorption of CO from $\text{CO}/\text{Cu}(111)$ is complete in less than 325 fs. [56]

We measured the desorption of O_2 and production of CO_2 from $\text{CO}/\text{O}_2/\text{Pt}(111)$ induced with 0.3-ps laser pulses at 267, 400, and 800 nm to determine the dependence of the chemical reaction on the electron distribution. We find that the reaction is sensitive to photon energy and therefore we favor excitation of the adsorbates by nonthermal electrons. We argue that the two-pulse correlation experiments have been misinterpreted; the correlation time reflects the time required for relaxation of adsorbate vibrational modes, rather than the substrate electron-phonon coupling time.

When the photochemistry of $\text{CO}/\text{O}_2/\text{Pt}(111)$ is induced with continuous light [28, 62] or nanosecond pulses, [51] the yields of O_2 and CO_2 scale linearly with fluence and depend strongly on photon energy. We report that the desorption induced by femtosecond laser pulses also scales linearly with fluence when the fluence is low. We observe the transition from linear to nonlinear dependence on fluence with 267- and 400-nm laser pulses.

V. A. Low-intensity photochemistry

Light from an arc lamp can induce desorption of O_2 from $\text{O}_2/\text{Pt}(111)$. Figure 52 shows the dependence of the O_2 desorption yield on photon wavelength. [28] The yield increases with decreasing wavelength and there is no photodesorption at wavelengths longer than 550 nm. Figure 53 shows that the desorption rate is linear in fluence: $Y \propto F^1$. Irradiation also induces rearrangement of the O_2 molecules on the surface; temperature programmed desorption following irradiation of $\text{O}_2/\text{Pt}(111)$ exhibits a broadened α - O_2 desorption peak compared to nonirradiated $\text{O}_2/\text{Pt}(111)$. [62, 63]

A model called DIET, for desorption induced by electron transitions, explains the wavelength dependence of the data and the linear dependence of yield on fluence. Figure 54 shows how electronic excitation of an adsorbate can cause it to acquire the translational energy required for desorption. In the electronic ground state the interaction of the adsorbate with the surface is described by the potential energy surface labeled PES_1 . The reaction coordinate could be, for example, the distance between the adsorbate and the surface, or the

alignment of the adsorbate with respect to the surface. The interaction of the adsorbate with the substrate following electronic excitation of the adsorbate is represented by the potential energy surface labeled PES_2 . In general, PES_2 does not have a minimum at the same reaction coordinate as PES_1 . PES_2 could be purely repulsive, with no minimum at all.

Electronic excitation of the adsorbate is represented by the vertical arrow from the minimum of PES_1 . This transition is an example of a Frank-Condon transition. The transition could be caused by a photon exciting an electron within the $O_2/Pt(111)$ complex; such an excitation does not change the overall charge on the adsorbate. The transition could also be the transfer of an electron from the substrate to the adsorbate, changing the charge on the adsorbate. If an electron is transferred to the adsorbate, the shape of PES_2 reflects the interaction between the charged adsorbate and the image charge in the substrate.

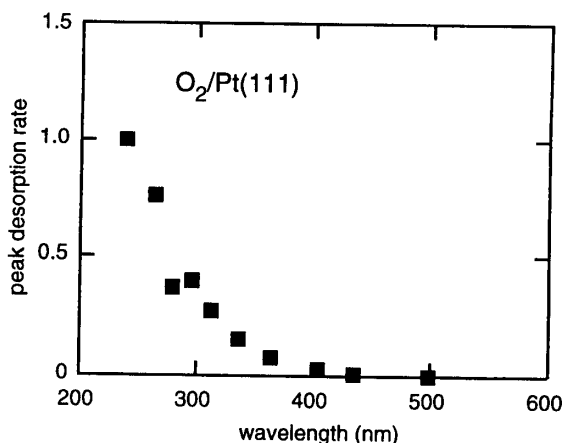


Figure 52 The rate of desorption of O_2 from $O_2/Pt(111)$ under irradiation with continuous light from an arc lamp. After [28]

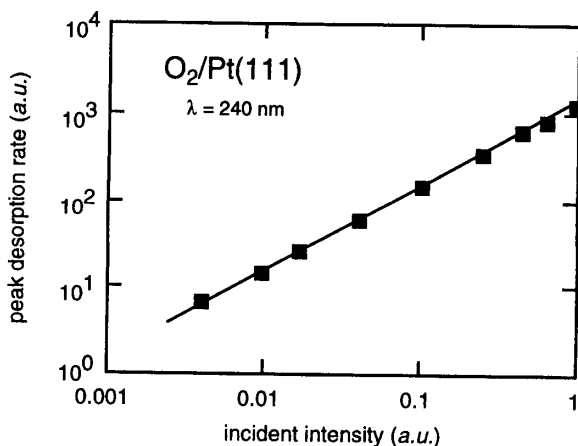


Figure 53 The rate of desorption of O_2 from $O_2/Pt(111)$ induced with 240 nm irradiation, as a function of the incident intensity. The line has slope 1. After [28]

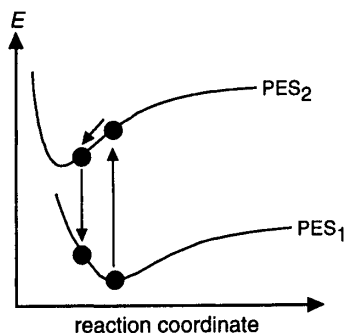


Figure 54 Desorption induced by electron transition (DIET) is explained in terms of two potential energy surfaces for the adsorbate-surface interaction.

An adsorbate excited to PES_2 accelerates towards the new potential energy minimum. When the electronic excitation relaxes, the adsorbate returns to PES_1 , having acquired translational and potential energy. This energy accounts for desorption of the adsorbate.

Each photo-excitation of an electron and the possible subsequent excitation of an adsorbate acts independently of the other photo-induced excitations. This feature of the model accounts for the linear dependence of yield on fluence. The dependence of yield on wavelength reflects the need for photo-excited electrons to have energies appropriate to access available affinity levels of the adsorbates.

During irradiation of $\text{O}_2/\text{Pt}(111)$ with an arc lamp, the fluence is kept low enough that the increase in surface temperature is only a few Kelvin: the surface temperature remains well below the 120 K temperature at which O_2 desorbs. According to the Fermi-Dirac function, Figure 25, the thermalized electron energies are near 20 meV. In contrast, the photon energy at, say, 400 nm, is about 3.2 eV. A photo-excited electron has an energy much greater than the thermal energy: it is these nonthermal electrons which govern the desorption. The nonthermal electrons have sufficient energy for the transition depicted in Figure 54. After thermalization of the electrons, the energy of an individual photon is distributed among all the electrons, and ultimately, all the surface modes. After thermalization, there is no longer sufficient energy in any individual electron to induce desorption.

The situation could be different when a subpicosecond laser pulses excites the material. According to Figure 38, the subpicosecond laser pulses creates a transient electron temperature far in excess of the temperature required for desorption of O_2 under equilibrium conditions. Could this hot, thermal distribution of electrons induce desorption? Our experiments are designed to address this question.

V. B. Subpicosecond laser desorption experiments

We studied the photochemistry of $\text{CO}/\text{O}_2/\text{Pt}(111)$ using laser pulses from a 1-kHz regeneratively-amplified Ti:sapphire laser. The 100-fs, 800-nm pulses are frequency-doubled in a 1-mm thick lithium barium borate crystal and frequency-tripled in a 0.3-mm thick beta-barium borate crystal. The laser pulse energy is varied with a waveplate and a polarizing beam splitter. The 267- and 400-nm pulses have 0.26- and 0.3-ps duration, respectively. The 800-nm pulses are chirped to 0.3 ps so the pulse durations at all wavelengths are similar.

The energy of each laser pulse is measured with a photodiode that is calibrated with a power meter. The response of the power meter varies less than 3% over the range 267–800 nm. To ensure that there is no nonlinear absorption in the platinum, we measured the fraction of the laser pulse energy absorbed into platinum. The measured absorption of the platinum is constant over the range of fluences used in the experiments, and is in agreement with the reflectivity calculated from the published dielectric function of platinum.[12] We also verified that the absorption of the chamber window does not depend on fluence. These results confirm that the laser energy absorbed in the platinum is a constant fraction of the pulse energy measured outside the vacuum chamber.

The spatial profile of the laser pulses is measured with an ultraviolet-sensitive CCD camera. The profile captured by the camera is fit well by a Gaussian function. The fluence incident on the camera is reduced to a level where the camera response is linear by reflecting the beam off the front surfaces of two pieces of glass and is further attenuated with neutral-density filters. To confirm the accuracy of the camera-based spatial profile measurement, we measured the spatial profile of a Helium-Neon laser with the camera and compared it with the profile determined by scanning a pinhole through the beam while measuring the transmitted light with a photodiode. The camera and pinhole methods yield laser profiles that are identical to within 1%.

The absorbed laser fluence is determined from the energy absorbed in the platinum, and the spatial profile of the laser pulse, accounting for the 45° angle of incidence. The fluence varies over the profile of the laser spot; values quoted below refer to the absorbed fluence at the peak of the spatial profile. The tests described above confirm that there is no wavelength-dependent, nor any fluence-dependent systematic error in the calculation of absorbed fluence.

The experiments are conducted on a 12-mm diameter Pt(111) crystal in an ultrahigh vacuum chamber with a base pressure of 5×10^{-11} torr. All experiments are performed at a base temperature of 84 K. The crystal is cleaned using Ne ion sputtering at an ion energy of 500 eV, annealing in vacuum at 1100 K, and annealing in 10^{-8} torr oxygen at 500–1000 K.[22] Surface order is verified with low-energy electron diffraction and surface cleanliness is verified with Auger spectroscopy.[63]

After cleaning, molecular oxygen and carbon monoxide are adsorbed to saturation on the platinum surface.[27, 28] Molecular oxygen is deposited on the platinum surface as soon as the temperature has fallen below 94 K after a cleaning cycle. Carbon monoxide is deposited after the oxygen. To reduce background pressure, all adsorbates are deposited using a tube of 12-mm diameter brought to within 3 mm of the platinum surface.

The laser-induced O₂ desorption yield and CO₂ reaction yield are measured with a quadrupole mass spectrometer operating in pulse-counting mode. We alternate between detecting O₂ and CO₂ on successive laser shots. Between shots, we translate the sample to an unirradiated part of the sample. A potential difference of –90 V is applied between the sample and the ionizer of the mass spectrometer to prevent stray electrons from interacting with the sample. A tube of 4-mm inner diameter extends from the ionizer to the sample. This tube collects molecules desorbed from the surface within 14° of the surface normal. Using a high-speed mechanical shutter, we reduce the laser repetition rate to allow the gas-phase products to be pumped out of the chamber between successive laser shots.

The yield depends on the area of the sample preparation exposed to the laser pulses. To obtain an appreciable yield at low fluence, a large laser spatial profile of full-width-half-maximum up to 1 mm² is used. At high fluence, the spatial profile is decreased to as low as

0.05 mm² to reduce the absolute yield and to avoid saturating the pulse-counting electronics. The yields reported below are divided by the laser spot size to allow comparison between runs taken with different laser spot sizes. Below 20 $\mu\text{J}/\text{mm}^2$, less than 1% of the adsorbates is depleted by a single laser pulse; to increase the signal in this regime, we admit up to 10 pulses at a 1-kHz rate to one spot on the sample and the mass spectrometer measures the total yield.

V. C. Results of the subpicosecond laser desorption experiments

Figure 55 shows the yield of oxygen molecules obtained from CO/O₂/Pt(111) with 267-, 400-, and 800-nm laser pulses. Near 10 $\mu\text{J}/\text{mm}^2$ there is a clear change in the dependence of the yield on absorbed laser fluence. Above 50 $\mu\text{J}/\text{mm}^2$, the yield saturates because the pulse desorbs an appreciable fraction of the adsorbed oxygen.[52]

Below 10 $\mu\text{J}/\text{mm}^2$ the yield from 267- and 400-nm pulses depends linearly on fluence. To determine the linear cross section in this regime, we measured the decreasing yield from a single spot on the sample as the surface coverage is depleted by 3,000 laser pulses. The linear cross sections thus obtained are $\sigma_{267} = (4 \pm 2) \times 10^{-23} \text{ m}^2$ and $\sigma_{400} = (4 \pm 2) \times 10^{-24} \text{ m}^2$ for 267- and 400-nm pulses, respectively. We do not observe any linear dependence of yield on fluence for 800-nm laser pulses; continuous light sources with wavelengths longer than 600 nm also do not induce reaction[28].

Between 10 and 50 $\mu\text{J}/\text{mm}^2$ the yield depends nonlinearly on fluence. The data can be described by a simple power law, $Y \sim F^p$, where $p > 1$ and F is the fluence absorbed in the platinum. As Table 1 shows, the exponent p decreases with decreasing wavelength.

The wavelength dependence of the yields is also apparent in a comparison of the absolute yields at a particular fluence. Table 2 summarizes the wavelength dependence of the yields at 1 and 30 $\mu\text{J}/\text{mm}^2$. At both fluences, the yield increases substantially as the wavelength decreases.

Figure 56 shows the yield of carbon dioxide from the same sample preparation as Figure

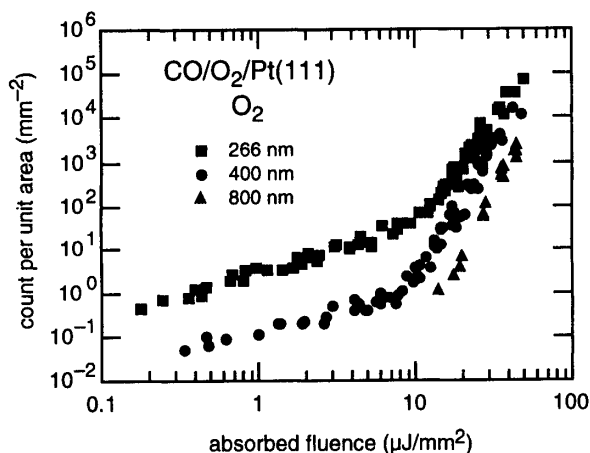


Figure 55 Yields of O₂ from CO/O₂/Pt(111) obtained with laser pulses of 0.3-ps duration at ▲ 800-, ● 400-, and ■ 267-nm wavelengths.

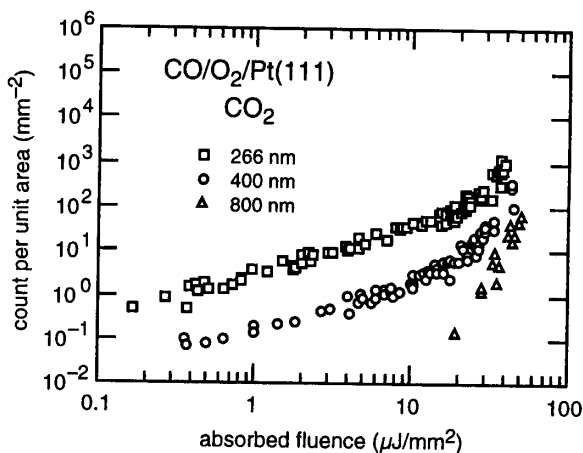


Figure 56 Yields of CO_2 from $\text{CO/O}_2/\text{Pt}(111)$ obtained with laser pulses of 0.3-ps duration at \triangle 800-, \circ 400-, and \square 267-nm wavelengths.

55. The dependence of the CO_2 yield on fluence is similar to that of O_2 . Table 3 summarizes the ratio of yield of O_2 to yield of CO_2 . When using 267- or 400-nm pulses at fluences below $10 \mu\text{J}/\text{mm}^2$ (*i.e.*, in the linear regime), the yields of O_2 and CO_2 are the same. Above $20 \mu\text{J}/\text{mm}^2$, the yield of O_2 is substantially more than the yield of CO_2 , and the ratio is smaller at shorter wavelengths. The ratios shown in Table 3 are not corrected for the small dependence of the mass spectrometer detection efficiency on species.

To explore the time dependence of the desorption, we measured the total desorption yield from two 80-fs laser pulses as a function of the delay $t_1 - t_2$ between them. The pulses are orthogonally polarized to avoid interference. The resulting two-pulse correlation is shown in Figure 57. The dashed line shows the total yield when the two pulses act independently, *i.e.*, when $t_1 - t_2 \rightarrow \pm\infty$. The dependence of the signal on $t_1 - t_2$ reflects the evolution of the substrate and adsorbate excitations responsible for desorption. The data show a 1.8 ps wide peak centered at $t_1 - t_2 = 0$ on top of broad wings. The broad wings are approximately 0.1 ns wide.

V. D. Discussion

The desorption and reaction yields at fluences below $10 \mu\text{J}/\text{mm}^2$, shown in Figures 55 and 56, scale linearly in fluence. The cross sections are about 10^{-23} m^2 and increase with decreasing wavelength. The yield of O_2 and CO_2 obtained from $\text{CO/O}_2/\text{Pt}(111)$ with continuous light[28] or nanosecond-pulses[51] also scales linearly in fluence. The cross sections measured with these low-intensity sources are about 10^{-23} m^2 and increase with decreasing wavelength. These similarities suggest that the linear surface femtochemistry is due to the same mechanism responsible for the surface photochemistry induced with continuous-wave or nanosecond-pulsed light sources.

The excitation of $\text{CO/O}_2/\text{Pt}(111)$ with these low-intensity sources has been attributed to electronic transitions into normally-vacant orbitals of the O_2 . [28] As discussed above, this new electronic configuration causes the adsorbate atoms to move, accumulating vibrational or

Table 1 Wavelength dependence of the power law exponent. The yield is linear in fluence below $10\text{ }\mu\text{J}/\text{mm}^2$, but very nonlinear in fluence above $10\text{ }\mu\text{J}/\text{mm}^2$. There is no low-fluence yield with 800-nm laser pulses.

<i>P</i>	267 nm	400 nm	800 nm
$\leq 10\text{ }\mu\text{J}/\text{mm}^2$	1.1 ± 0.1	0.9 ± 0.1	n.a.
$\geq 10\text{ }\mu\text{J}/\text{mm}^2$	4.8 ± 0.5	6.0 ± 0.5	7.2 ± 0.5

Table 2 Wavelength dependence of the laser-induced yield. At all fluences studied, the yield increases with decreasing wavelength.

yield	267 nm	400 nm	800 nm
$1\text{ }\mu\text{J}/\text{mm}^2$	3 ± 0.5	0.1 ± 0.02	0
$30\text{ }\mu\text{J}/\text{mm}^2$	8000 ± 1500	2000 ± 500	120 ± 25

Table 3 Wavelength dependence of the ratio of O₂ to CO₂ yield. The ratio is one at fluences below $10\text{ }\mu\text{J}/\text{mm}^2$, but O₂ desorption is favored over production of CO₂ at fluences above $20\text{ }\mu\text{J}/\text{mm}^2$. At fluences above $20\text{ }\mu\text{J}/\text{mm}^2$, the ratio is strongly wavelength dependent.

O ₂ :CO ₂	267 nm	400 nm	800 nm
$\leq 10\text{ }\mu\text{J}/\text{mm}^2$	1 ± 0.1	1 ± 0.1	n.a.
$\geq 20\text{ }\mu\text{J}/\text{mm}^2$	25 ± 5	55 ± 15	70 ± 10

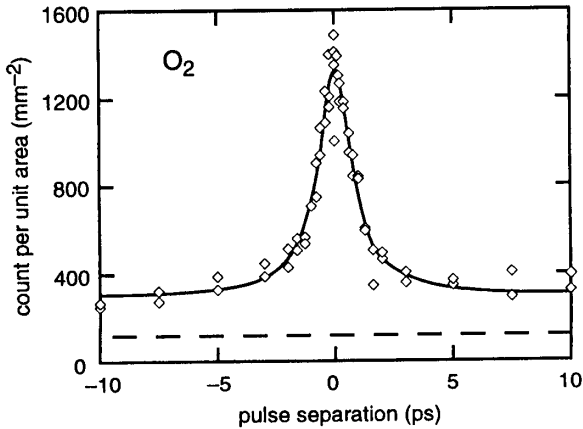


Figure 57 Desorption yield versus time delay $t_1 - t_2$ between two 80-fs excitation pulses at 800-nm for pulses of equal absorbed fluences. The dashed line denotes $Y(t_1 - t_2 = \pm\infty)$. The width of the central peak is 1.8 ps. The desorption yield is still enhanced after 75 ps.[52]

translational energy that may lead to desorption or reaction. Two mechanisms for the electronic transition have been proposed. The photon can stimulate a direct transition between orbitals in the $\text{O}_2/\text{Pt}(111)$ complex.[28] Alternatively, the photon may excite an electron to a state above the Fermi level in the $\text{Pt}(111)$ band structure, from which it crosses into an orbital of the $\text{O}_2/\text{Pt}(111)$ complex.[64] Either way, the electron interacts with the O_2 while retaining a substantial portion of the initial photon energy. The surface photochemistry in the linear regime is therefore governed by electrons with a nonthermal distribution. The wavelength dependence of the cross section is due to the required matching of the energy of the photo-excited electron with the energies of the vacant O_2 orbitals.

Irradiation of a metal surface creates an electron distribution with thermal and nonthermal components. As indicated in Figure 39, after intense subpicosecond laser pulses excite a metal, the thermal distribution of electrons that can be several thousand Kelvin for a few picoseconds.[49] Several authors attribute the nonlinear dependence of yield on fluence, high desorption yields, and short excitation lifetimes to these transient hot electrons.[57, 65-67] The electron temperature depends on the pulse duration and the fluence absorbed in the platinum, but not on photon wavelength.[14]

Our experiments show three ways in which the nonlinear surface femtochemistry depends on wavelength. The power-law exponents summarized in Table 1 depend on wavelength, increasing from 4.8 ± 0.5 at 267 nm to 7.2 ± 0.5 at 800 nm. The desorption yields summarized in Table 2 are also wavelength dependent: at $30 \mu\text{J}/\text{mm}^2$, the yield from 267-nm pulses is about 4 times that from 400-nm pulses, and about 65 times that from 800-nm pulses. The ratio between O_2 and CO_2 yields, summarized in Table 3, depends on wavelength, varying from 70 at 800 nm to 25 at 267 nm. The nonlinear femtochemistry of $\text{CO}/\text{O}_2/\text{Pt}(111)$ depends on wavelength, and so the thermalized electron distribution cannot be solely responsible for exciting the adsorbates. We attribute the wavelength dependence of the nonlinear surface femtochemistry on $\text{CO}/\text{O}_2/\text{Pt}(111)$ to interaction of the adsorbates with electrons from a nonthermal (non Fermi-Dirac) distribution.

The data from the two-pulse correlation experiments, Figure 57, show that the sample retains excitation from the first laser pulse for longer than 10 ps. This correlation time is longer than the electron-electron, electron-adsorbate,[55, 67] electron-lattice,[15, 49] and lattice-adsorbate[29, 30] relaxation times. The only remaining equilibration process is the cooling of the surface to the bulk, which occurs on roughly the same time scale as the decay of the wings. The correlation beyond 10 ps indicates that desorption is accomplished more easily from a pre-heated surface than from a cold surface.

We consider now the prominent 1 ps wide peak in Figure 57.[52, 61] Experiments show that in subpicosecond laser excitation of gold film, the nonthermal electron distribution persists for 0.5 ps.[16, 68] Though there are no published measurements of the electron-electron thermalization time for platinum, the thermalization time in platinum is likely less than the 1 ps correlation in Figure 57. It is therefore unlikely that the 1 ps correlation reflects the time for electrons to thermalize.

The 1 ps correlation in Figure 57 has been attributed to cooling of the thermalized electron distribution,[50, 59, 61] because, as Figure 39 shows, the electrons equilibrate with the lattice on a 1 ps time scale. Though the thermalized electron distribution may contribute to the laser-induced desorption and contribute to the 1 ps correlation, the wavelength dependence of our data indicates that thermalized electrons do not solely govern the desorption. The 1 ps correlation more likely reflects the time required for the adsorbates to dissipate the vibrational

excitation induced by the first laser pulse. Indeed, the time scale for relaxation of vibrational excitation at a metal surface is approximately 1 ps.[29, 30]

V. E. Conclusions from the surface femtochemistry experiments

The absolute and relative cross sections for desorption and reaction depend on fluence. At high fluence, where desorption is more efficient than reaction, adsorbates can be desorbed with subpicosecond time-resolution for analysis. The efficient desorption could also be used to create empty reactive sites and increase reaction rate in a catalytic process in which site blocking inhibits the reaction. Finally, because the linear surface femtochemistry is caused by the same mechanism as the surface photochemistry induced with continuous light, the dynamics of the surface photochemistry induced with continuous light can be studied with femtosecond time-resolution by limiting the femtosecond pulses to low fluence.

The transition between nonlinear and linear surface femtochemistry is also of theoretical interest. At low fluence, the linear dependence of yield on fluence is due to desorption or reaction caused by a single electronic excitation. Above the transition fluence, the nonlinearity indicates that cooperative action of the photo-excited electrons dominates the linear process. These cooperative effects have been described as a frictional coupling between the substrate electrons and the adsorbates,[66] and as a repeated excitation of the adsorbate within the time required for cooling of the adsorbate vibration[67].

We describe the surface femtochemistry of $\text{O}_2/\text{CO}/\text{Pt}(111)$ as follows. Linear surface femtochemistry, observed at fluences below $10 \mu\text{J}/\text{mm}^2$, is due to the same mechanism as surface photochemistry induced with continuous-wave and nanosecond pulses. Above $10 \mu\text{J}/\text{mm}^2$, another excitation mechanism dominates the reaction; yields are nonlinear in fluence and depend on wavelength.

It is not correct to completely attribute the desorption and reaction yields to the influence of a thermalized electron distribution, such as depicted in Figure 39. Models need to account for the nonthermal electrons to predict the wavelength dependence of our data. This result implies that previously-published two-pulse correlation data must be re-interpreted. The short, 10^{-12} -s correlation is due to relaxation of vibrational excitation of the adsorbates between laser pulses, and not due to cooling of the electrons to the bulk phonon temperature.

VI. REFERENCES

1. J. J. Sakurai, *Modern quantum mechanics*. S. F. Tuan, Ed. (Addison-Wesley, New York, 1985).
2. P. W. Atkins, *Molecular quantum mechanics* (Oxford University Press, Oxford, ed. 2nd, 1983).
3. C. Cohen-Tannoudji, B. Diu, F. Laloë, *Quantum mechanics* (John Wiley and Sons, New York, 1977), vol. 2.
4. M. Tinkham, *Group theory and quantum mechanics* (McGraw-Hill, New York, 1964).
5. J. D. Jackson, *Classical Electrodynamics* (John Wiley and Sons, New York, ed. Second Edition, 1962).
6. R. Shen, *The principles of nonlinear optics* (Wiley Interscience, New York, 1984).
7. C. Kittel, *Introduction to Solid State Physics* (John Wiley and Sons, New York, ed. 6th, 1986).

8. N. W. Ashcroft, N. D. Mermin, *Solid state physics*. D. G. Crane, Ed. (Saunders College, Philadelphia, 1976).
9. B. Segall, *Phys. Rev.* **124**, 1797 (1961).
10. G. A. Burdick, *Phys. Rev.* **129**, 138 (1963).
11. G. Leschik, R. Courths, H. Wern, S. Hüfner, H. Eckardt, J. Noffke, *Solid State Comm.* **52**, 221-225 (1984).
12. J. H. Weaver, C. Krafka, D. W. Lynch, E. E. Koch, *Optical Constants of Materials, Part I, Physics Data* (1981).
13. P. N. Ray, J. Chowdhuri, S. Chatterjee, *J. Phys. F* **13**, 2569-2580 (1983).
14. S. I. Anisimov, B. L. Kapeliovich, T. L. Perel'man, *Sov. Phys. JETP* **39**, 375 (1974).
15. P. B. Corkum, F. Brunel, N. K. Sherman, T. Srinivasan-Rao, *Phys. Rev. Lett.* **61**, 2886-2889 (1988).
16. C. Suárez, W. E. Bron, T. Juhasz, *Phys. Rev. Lett.* **75**, 4536-4539 (1995).
17. W. S. Fann, R. Storz, H. W. K. Tom, J. Bokor, *Phys. Rev. Lett.* **68**, 2834-2837 (1992).
18. S. Ogawa, H. Petek, *Surf. Sci.* **357-358**, 585-594 (1996).
19. C.-K. Sun, F. Vallée, L. H. Acioli, E. P. Ippen, J. G. Fujimoto, *Phys. Rev. B* **50**, 15337-15347 (1994).
20. B. Feuerbacher, B. Fitton, R. F. Willis, Eds., *Photoemission and the electronic properties of surfaces* (Wiley, New York, 1978).
21. H. Lüth, *Surfaces and interfaces of solids*. G. Ertl, R. Gomer, D. L. Mills, Eds., Springer Series in Surface Science (Springer-Verlag, Berlin, 1993), vol. 15.
22. R. G. Musket, W. McLean, C. A. Colmenares, D. M. Makowiecki, W. J. Siekhaus, *Applications of Surf. Sci.* **10**, 143-207 (1982).
23. E. M. Purcell, *Electricity and magnetism*, Berkeley Physics Course (McGraw-Hill Book Company, New York, ed. 2, 1985).
24. J. Grimblot, A. C. Luntz, D. E. Fowler, *Journal of electron spectroscopy and related phenomena* **52**, 161-174 (1990).
25. L. E. Davis, N. C. MacDonald, P. W. Palmberg, G. E. Riach, R. E. Weber, *Handbook of auger electron spectroscopy* (Physical Electronics Industries, Inc., Eden Prairie, ed. 2nd, 1976).
26. H. Steininger, S. Lehwald, H. Ibach, *Surface Science* **123**, 1-17 (1982).
27. J. Gland, V. Serton, G. Fisher, *Surface Science* **95**, 587-602 (1980).
28. W. D. Miehler, W. Ho, *J. Chem. Phys.* **99**, 9279-9295 (1993).
29. T. A. Germer, J. C. Stephenson, E. J. Heilweil, R. R. Cavanagh, *Phys. Rev. Lett.* **71**, 3327 (1993).
30. T. A. Germer, J. C. Stephenson, E. J. Heilweil, R. R. Cavanagh, *J. Chem. Phys.* **101**, 1704 (1994).
31. J. Winterlin, R. Schuster, G. Ertl, *Phys. Rev. Lett.* **77**, 123-126 (1996).
32. J. Gland, E. Kollin, *J. Chem. Phys.* **78**, 963-974 (1983).
33. T. Matsushima, *Surf. Sci.* **127**, 403-423 (1983).
34. K.-H. Allers, H. Pfnür, P. Feulner, D. Menzel, *J. Chem. Phys.* **100**, 3985-3998 (1994).
35. M. Orchin, H. H. Jaffé, *Symmetry, Orbitals, and Spectra (S.O.S.)* (Wiley-Interscience, New York, 1971).
36. B. C. Stipe, M. A. Rezaei, W. Ho, S. Gao, M. Persson, B. I. Lundqvist, *Phys. Rev. Lett.* **78**, 4410-4413 (1997).
37. A. Eichler, J. Hafner, *Phys. Rev. Lett.* **79**, 4481-4484 (1997).

38. W. Eberhardt, T. H. Upton, S. Cramm, L. Incoccia, *J. Vac. Sci. Tech. A* **6**, 876-877 (1988).
39. W. Wurth, et al., *Phys. Rev. Lett.* **65**, 2426-2429 (1990).
40. J. L. Gland, V. N. Korchak, *Surf. Sci.* **75**, 733 (1978).
41. A. W. E. Chan, R. Hoffmann, W. Ho, *Langmuir* **8**, 1111-1119 (1992).
42. D. A. Outka, J. Stöhr, W. Jark, P. Stevens, J. Solomon, R. J. Madix, *Phys. Rev. B* **35**, 4119-4122 (1987).
43. B. Hellsing, *Surf. Sci.* **282**, 216-228 (1993).
44. I. Panas, P. Siegbahn, *Chem. Phys. Lett.* **153**, 458-464 (1988).
45. N. V. Smith, *Phys. Rev. B* **9**, 1365 (1974).
46. N. Avery, *Chem. Phys. Lett.* **96**, 371-373 (1983).
47. K. Mortensen, C. Klink, F. Jensen, F. Besenbacher, I. Stensgaard, *Surface Science* **220**, L701-L708 (1989).
48. K. Sawabe, Y. Matsumoto, *Chem. Phys. Lett.* **194**, 45-50 (1992).
49. J. A. Prybyla, T. F. Heinz, J. A. Misewich, M. M. T. Loy, J. H. Glowina, *Phys. Rev. Lett.* **64**, 1537-1540 (1990).
50. F. Budde, T. F. Heinz, M. M. T. Loy, J. A. Misewich, F. de Rougemont, H. Zacharias, *Phys. Rev. Lett.* **66**, 3024-3027 (1991).
51. F.-J. Kao, D. G. Busch, D. G. da Costa, W. Ho, *Phys. Rev. Lett.* **70**, 4098-4101 (1993).
52. S. Deliwala, R. J. Finlay, J. R. Goldman, T. H. Her, W. D. Mieher, E. Mazur, *Chem. Phys. Lett.* **242**, 617-622 (1995).
53. R. J. Finlay, T.-H. Her, C. Wu, E. Mazur, *Chem. Phys. Lett.* **274**, 499-504 (1997).
54. D. G. Busch, W. Ho, *Phys. Rev. Lett.* **77**, 1338-1341 (1996).
55. F. Budde, T. F. Heinz, A. Kalamarides, M. M. T. Loy, J. A. Misewich, *Surf. Sci.* **283**, 143-157 (1993).
56. J. A. Prybyla, H. W. K. Tom, G. D. Aumiller, *Phys. Rev. Lett.* **68**, 503-506 (1992).
57. L. M. Struck, L. J. Richter, S. A. Buntin, R. R. Cavanagh, J. C. Stephenson, *Phys. Rev. Lett.* **77**, 4576-4579 (1996).
58. R. J. Finlay, S. Deliwala, J. R. Goldman, T. H. Her, W. D. Mieher, C. Wu, E. Mazur, in *Laser Techniques for Surface Science II* . (1995), vol. 2547, pp. 218-226.
59. J. A. Misewich, A. Kalamarides, T. F. Heinz, U. Höfer, M. M. T. Loy, *J. Chem. Phys.* **100**, 736-739 (1994).
60. D. G. Busch, S. Gao, R. A. Pelak, M. F. Booth, W. Ho, *Phys. Rev. Lett.* **75**, 673-676 (1995).
61. F.-J. Kao, D. G. Busch, D. Cohen, D. G. da Costa, W. Ho, *Phys. Rev. Lett.* **71**, 2094-2097 (1993).
62. X.-Y. Zhu, S. R. Hatch, A. Champion, J. M. White, *J. Chem. Phys.* **91**, 5011-5020 (1989).
63. C. E. Tripa, C. R. Arumaninayagam, J. T. Yates, *J. Chem. Phys.* **105**, 1691-1696 (1996).
64. F. Weik, A. de Meijere, E. Hasselbrink, *J. Chem. Phys.* **99**, 682 (1993).
65. W. Ho, *Surf. Sci.* **363**, 166-178 (1996).
66. C. Springer, M. Head-Gordon, *Chem. Phys.* **205**, 73-89 (1996).
67. J. A. Misewich, T. F. Heinz, D. M. Newns, *Phys. Rev. Lett.* **68**, 3737-3740 (1992).
68. W. S. Fann, R. Storz, H. W. K. Tom, J. Bokor, *Surf. Sci.* **283**, 221-225 (1993).